Investigation of Deformable Image Registration Based Lung Ventilation Mapping for Radiation Therapy Using a Hybrid Hyperpolarized Gas MRI Technique

by

Isabella Duarte

Graduate Program in Medical Physics
Duke University

Date:_____

Approved:

_____
Jing Cai, Supervisor

_____
Fang-Fang Yin, Supervisor

_____
Lei Ren, Chair

_____
Bastiaan Driehuys

_____
Christopher Kelsey

Dissertation submitted in partial fulfillment of the requirements for the degree of Doctor of Philosophy in the Graduate Program in Medical Physics in the Graduate School of Duke University

2020

ABSTRACT

Investigation of Deformable Image Registration Based Lung Ventilation Mapping for Radiation Therapy Using a Hybrid Hyperpolarized Gas MRI Technique

by

Isabella Duarte

Graduate Program in Medical Physics
Duke University

Date:_____
Approved:

_____
Jing Cai, Supervisor

_____
Fang-Fang Yin, Supervisor

_____
Lei Ren, Chair

_____
Bastiaan Driehuys

_____
Christopher Kelsey

An abstract of a dissertation submitted in partial fulfillment of the requirements for the degree of Doctor of Philosophy in the Graduate Program in Medical Physics in the Graduate School of Duke University

2020

Abstract

Radiation-induced pulmonary toxicity poses a serious challenge and limiting factor in delivering a sufficient amount of dose to eradicate thoracic tumors without compromising lung function. Functional avoidance radiation therapy (RT) using lung ventilation mapping techniques would allow for preferential avoidance of functional lung tissue during radiotherapy and potentially reduce RT-induced lung injuries. Additionally, lung ventilation is also a key metric to assess lung function in patients with pulmonary diseases such as asthma, pulmonary embolism, cystic fibrosis, and chronic obstructive pulmonary disease (COPD). In contrast to global pulmonary function tests such as spirometry, ventilation images provide a regional measure of pulmonary function. Conventional methods for lung ventilation imaging include gamma camera scintigraphy and positron emission tomography scan after inhaling a gaseous radionuclide, as well as hyperpolarized (HP) gas magnetic resonance imaging (MRI) using Helium-3 and Xenon-129 as imaging contrast. Recently, a new method has been proposed in which deformable image registration (DIR) is performed on a pair of anatomical lung images at different respiratory phases to obtain the displacement vector field (DVF) between both phases, and generate a lung ventilation map from the Jacobian Determinant of the DVF. This DIR-based method is advantageous in its high image resolutions and simpler imaging procedures making it a more feasible option for implementation into the clinical workflow. However, current DIR-based lung ventilation

methods have been largely hampered due to two major deficiencies: 1) current DIR algorithms are morphologically based, lacking of sufficient physiological realism and thus resulting in erroneous calculations of lung ventilation; and 2) there is a lack of validation of the DIR-based lung ventilation calculation against clinical ground truth, as well as large uncertainties and variations among different DIR algorithms. The *long-term goal* of this proposal is to develop the necessary tools and metrics for validation and testing of DIR-based lung ventilation mapping techniques to contribute to their clinical implementation in advanced radiotherapy of lung cancer and diagnosis of obstructive pulmonary diseases. The *objective* of the proposed research is to develop physiologically-plausible respiratory motion models as a valuable tool for validation of DIR algorithms, and evaluate deformation-based lung ventilation mapping techniques against reference HP gas MRI ventilation images. The specific aims of this dissertation are the following. (1) Develop digital thoracic phantoms based on physiological modeling of respiratory motion from hyperpolarized gas tagging MRI. (2) Investigate the differences between HP gas tagging-based, DIR-based, and HP MRI ventilation mapping methods. (3) Evaluate and compare the sensitivity to deformation changes of ventilation and strain as lung functionality metrics.

This study investigates a unique dataset which includes three types of MR images acquired using a novel hybrid MRI technique in a single breath-hold maneuver

including a HP Helium-3 ventilation image, a pair of proton MR images, and a pair of HP Helium-3 tagging images at end of inhalation (EOI) and end of exhalation (EOE).

In order to create a physiologically plausible lung motion model, we used the novel HP gas tagging MRI technique. The tagged elements in the 3-dimensional (3D) tagged grid pattern are essentially ~500 evenly distributed landmarks throughout the entire lung area. Therefore, the displacement vector field calculated by tracking their motion from the EOI to the EOE phases provided us with a true lung deformation model which is physiologically-based.

The respiratory motion model was utilized to evaluate DIR-based displacement vector fields. The mean absolute DVF differences were found to be 8.2 mm for Subject 1, 7.5 mm for Subject 2, 5.6 mm for Subject 3, and 8.8 mm for Subject 4. These results show that there can be significant differences in DVF when performing a DIR compared to the respiratory motion models created from the tagged elements' displacement.

The thoracic motion model was then created through a combination of the DIR-based DVF to model the deformation outside the lungs from the registration of proton MR images, and the tagging-based DVF to model deformation inside the lungs using the manually measured DVF from the tagging MR images.

The next part of this dissertation focused on investigating a DIR- based lung ventilation mapping technique using proton MR images by evaluating its correlation with hyperpolarized Helium-3 gas ventilation MRI reference images which provide a

ground-truth measure of lung ventilation. Correlation between the reference ventilation images and ventilation maps computed from HP gas tagging MRIs, which provide ground-truth lung deformation, was also investigated. This is the first study, to our knowledge, to investigate three types of ventilation maps that are all MR-based. Furthermore, all images/data used in our evaluation are acquired during one same breath hold maneuver, eliminating the uncertainties associated with reproducibility of the respiratory cycle, patient positioning, and finding the spatial correspondence between the ventilation maps being evaluated.

The results of the spatial comparison between the DIR-based and reference ventilation images showed moderate to strong spearman correlation coefficients which are higher than many previous ventilation evaluation studies in the literature This may also be due to the fact that the images in this study were acquired during the same breath-hold and therefore inherently co-registered. The tagging-based ventilation maps, which are independent of the accuracy of any DIR algorithms, showed very similar spatial correlations to the reference images compared to the DIR-based ventilation maps. This proves the potential of the Jacobian ventilation calculation method which assumes that local volume changes are an appropriate lung ventilation surrogate. As more RT clinics incorporate MR imaging for patient simulation, and contouring for treatment planning, this study shows the feasibility of utilizing MR images for DIR-based ventilation calculations.

In the final part of this dissertation, we investigate lung strain as an additional metric to assess respiratory mechanics. We evaluated the sensitivity to deformation changes of both ventilation and strain as lung functionality metrics by comparing both metrics' sensitivity to changes in displacement vector fields using Hyperpolarized He-3 Tagging MRI data. This study utilized physiologically-based respiratory motion models from three subjects to assess the sensitivity of lung strain and lung ventilation by introducing a number of modifications to the DVF, generating new lung function maps, and investigating how much each of these lung function metrics were affected. Lung strain was computed voxel-wise from the gradient of the tagging-based deformation field. Through this algorithm, we obtained a 3x3 tensor that directly measures both the magnitude and direction of the lung deformation and then determines the three principal strains. For the lung ventilation calculation, we used the previously described voxel-by-voxel algorithm which was based on computing the Jacobian Determinant of the tagging-based DVF to determine the local volume changes. These results show much larger mean absolute percent differences between original and modified ventilation maps compared to the principal strain maps for all tests performed in this study; ranging from an average of 49.5 to 2743.7% for ventilation and 30.6 to 650.0% for strain among the 3 subjects. The principal strain maps showed much smaller average standard deviations between subjects. We found that Tagging-based ventilation maps calculated through the Jacobian of the DVF might be more sensitive to deformation changes

compared to the lung strain maps, showing much larger mean absolute percent differences between the original and modified maps. This could indicate two things, while ventilation might be more sensitive to smaller deformation changes which could be an advantage, this could also indicate that it is more sensitive to small errors or uncertainties in the DVF which could make the calculation more unstable compared to strain.

In conclusion, this dissertation utilized a unique hybrid MR image acquisition method to present: the development of valuable physiologically-based respiratory motion models and DIR validation tools using novel tagging MR images; the first all MR-based evaluation of deformation-based ventilation mapping techniques, against reference HP gas He-3 MR ventilation images with improved spatial correspondence; and the investigation of lung strain as an additional metric to assess lung function.

Dedication

I would like to dedicate this dissertation to my family who has given me their unconditional support throughout my entire career.

Contents

List of Tables

List of Figures

List of Abbreviations

%	Percent
AAPM	American Association of Physicists in Medicine
AI	Artificial Intelligence
AP	Anterior-Posterior
CA	California
CC	Cross Correlation
COPD	Chronic Obstructive Pulmonary Disease
CT	Computed Tomography
DIR	Deformable Image Registration
DNA	Deoxyribonucleic Acid
DTPA	Diethylenetriamine Pentaacetic Acid
DVF	Displacement Vector Field
EOE	End of Exhalation
EOI	End of Inhalation
FEV	Forced Expiratory Volume
fSAD	Functional Small Airway Disease
FVC	Forced Vital Capacity

He	Helium
HP	Hyperpolarized
HU	Hounsfield Unit
Hz	Hertz
IPF	Idiopathic Pulmonary Fibrosis
IRB	Institutional Review Board
LAT	Lateral
LINAC	Linear Accelerator
MI	Mutual Information
mm	Millimeter
MR	Magnetic Resonance
MRI	Magnetic Resonance Imaging
MSD	Mean Square Differences
NIH	National Institute of Health
NSCLC	Non-Small Cell Lung Cancer
OAR	Organ at Risk
PET	Positron Emission Tomography
PFT	Pulmonary Function Test
PRM	Parametric Response Mapping

RILI	Radiation Induced Lung Injury
RIR	Rigid Image Registration
ROI	Region of Interest
RT	Radiation Therapy
SI	Superior Inferior
SPECT	Single Photon Emission Computed Tomography
SSFP	Steady State Free Precession
TE	Time Echo
TG	Task Group
TR	Time Repetition
Xe	Xenon

Acknowledgements

I would like to thank my advisors Dr. Jing Cai and Dr. Fang-Fang Yin for their guidance and mentorship throughout my Ph.D. study. You have shaped me into a strong scientist and investigator and have always supported my professional and academic career goals. I would also like to thank our collaborators at the University of Virginia, especially Dr. Wilson Miller for his continuous support on image acquisitions, as well as his technical guidance and expertise. To the members of my committee, Dr. Lei Ren, Dr. Bastiaan Driehuys, and Dr. Christopher Kelsey for their feedback and expertise during my studies, preliminary examination and dissertation defense; you have all been key members in shaping the direction of this dissertation. Thank you to my classmates and labmates in the Duke Medical Physics Graduate Program as well as my labmates at the Hong Kong Polytechnic University, who have all played an important role in my Ph.D. study. Lastly, I would like to thank the leadership and administration of our program, for my excellent education and for allowing me to be part of numerous leadership positons, committees, and initiatives within the program.

1. Introduction

1.1 Significance and Motivation

Lung cancer is the leading cause of cancer deaths among men and women in the United States, and the second-leading cause of death in the country after heart disease.[1] In 2017, lung cancer caused more deaths than breast, prostate, brain and colorectal cancers combined, with a five-year relative survival rate of about 20%.[1] In addition to surgery and/or chemotherapy, radiation therapy (RT) is commonly utilized in the treatment of thoracic cancers. However, radiation-induced pulmonary toxicity affects a great number of patients receiving radiation therapy treatment for thoracic cancer, resulting in severe complications such as symptomatic pneumonitis and fibrosis.[2] This poses a serious challenge and limiting factor in delivering a sufficient amount of dose to eradicate thoracic tumors without compromising lung function. Ventilation is an important aspect of lung function, and has shown great promise for advanced radiotherapy of lung cancer. Lung ventilation mapping techniques would allow for preferential avoidance of functional lung tissue during radiotherapy and potentially reduce RT-induced lung injuries. Functional avoidance of lung tissue during radiotherapy treatment planning has been proposed as a method to significantly improve treatment outcomes of lung cancer by minimizing normal lung toxicity, and for adaptive radiotherapy by providing a mean to measure regional lung functional changes during radiation therapy treatment.[3–7] Being able to acquire a regional ventilation

measure would potentially allow for better personalized and more precise radiotherapy treatment for lung cancer. Additionally, lung ventilation is also a key metric to assess lung function in patients with pulmonary diseases such as asthma, pulmonary embolism, cystic fibrosis, and chronic obstructive pulmonary disease (COPD). Conventionally, these diseases are diagnosed through *global* pulmonary function tests such as spirometry. However, *regional* lung ventilation mapping techniques would allow us to diagnose these diseases at their earlier stages and monitor their progression.[8]

1.2 Background

1.2.1 Radiation Therapy Treatment

More than half of cancer patients will receive some type of radiation therapy treatment. External beam radiation therapy utilizes high energy electromagnetic radiation beams commonly created from a linear accelerator (LINAC) to target cancer cells. At very high doses, radiation therapy causes cancer cells to stop dividing or die by severely damaging their DNA. The RT treatment chain consists of three main components: (1) patient immobilization and imaging for treatment simulation, (2) tumor localization and treatment planning, and (3) patient positioning and treatment delivery. The main goal of radiation therapy is to deliver a high dose of radiation to the tumor or target while minimizing and limiting dose to healthy tissue or surrounding organs at risk (OARs). Cancer cells and OARs have varying radiation sensitivities, and thus radiation treatment plans are designed and optimized to limit side effects and radiation-

induced toxicities to the surrounding organs, while maintaining adequate dose and coverage to the target. Therefore, all steps in the treatment chain are key in ensuring an accurate treatment delivery.

1.2.1.1 Radiation-Induced Lung Injuries

Radiation-induced lung injury (RILI) is the most common complication following thoracic radiotherapy treatments. As mentioned before, these possible lung toxicities become a major dose-limiting factor in order to eradicate thoracic tumors without compromising lung function. RILI can develop as radiation pneumonitis and pulmonary fibrosis. Radiation pneumonitis is an inflammation in the lung tissue and represents an acute phase of RILI; its onset can occur approximately 1-6 months after radiation therapy treatment. The inflammation of the alveoli causes the tissue to deteriorate which can cause the lung tissue to become fibrotic or permanently scarred. Pulmonary fibrosis is characterized by scarring in the lung tissue, and it represents a late and chronic phase of radiation-induced pulmonary toxicity and has an onset that can vary from months to years after treatment.[9] Pulmonary fibrosis is progressive and irreversible, and as the tissue in the alveoli becomes scarred and stiff, patients begin to have difficulty breathing as it becomes harder for oxygen to pass through the alveoli and into the bloodstream. These injuries can have a severe effect on the quality of life of thoracic cancer patients and largely hamper dose-escalation efforts to increase local control and improve treatment outcomes of advanced non-small cell lung cancer

(NSCLC). Therefore, recent studies have investigated the use of functional avoidance radiotherapy to potentially reduce radiation-induced toxicity in lung cancer patients.[10]

1.2.1.2 Functional Avoidance Treatment Planning

Current radiation therapy treatment planning techniques aim to minimize radiation dose to the total lung volume and do not account for regional variations in lung function.[10–12] However, lung function has shown to be heterogeneous for smokers and patients with pulmonary diseases. Therefore, functional avoidance treatment planning aims to minimize dose deposition to high-functioning areas of the lungs by favoring dose deposition to the less- functioning areas (see Figure 1), in order to potentially reduce RILI and improve treatment outcomes.[10–12] Studies have investigated the impact that functional avoidance radiation therapy could have in decreasing the probability of toxicities.[10,11] There are several metrics and imaging modalities that can be used to assess lung function and its regional variations which will be discussed in this dissertation.

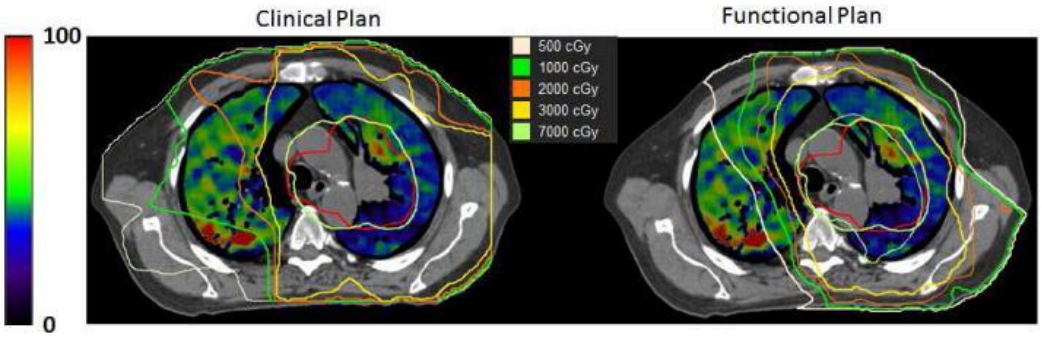

Figure 1: Example of a clinical radiation therapy plan compared to a functional avoidance plan.In the functional plan, the dose deposition to the higher-functioning regions of the lung has been minimized as shown by the overlaid isodose lines.[10]

1.2.2 Lung Function

The primary function of the lungs is the process of *gas exchange* which is defined as the exchange of oxygen and carbon dioxide between the alveoli in the lungs and the blood in the capillaries as described in Figure 2. The three main processes to transfer oxygen into the bloodstream are:

1. **Ventilation**: the exchange or flow of air between the lungs and the atmosphere (i.e. airflow in the lungs).
2. **Perfusion**: the flow of blood in the pulmonary capillaries (i.e. blood flow in the lungs).
3. **Diffusion**: the spontaneous movement of gases between the alveoli and the blood in the capillaries. The respiratory membrane is very permeable, and the

exchange of gases is a spontaneous movement that occurs due to simple diffusion from gases following pressure gradients.

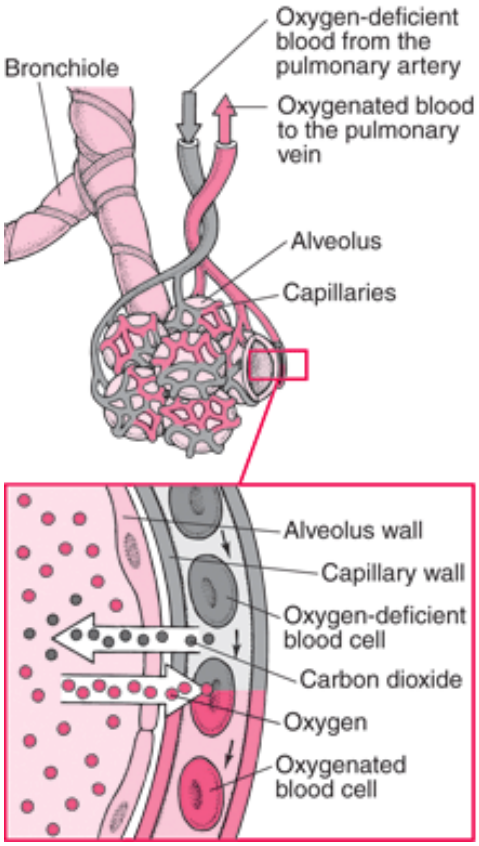

Figure 2: Gas exchange process between the alveoli and the capillaries in the lungs.[13]

1.2.2.1 Pulmonary Function Tests

There are several methods that are currently clinically employed to measure lung function. Pulmonary function tests (PFTS) are an important tool in monitoring and

aiding in the diagnosis of pulmonary diseases. The most frequently used PFT is spirometry, which measures the volume and the speed or flow in which the air can be moved in and out of the lungs (i.e. volume as a function of time). The procedure consists of a forced vital capacity maneuver in which the patient takes a maximal inspiration and then forcefully expels the air into a mouthpiece.[14] The mouthpiece is connected to the spirometer which calculates the patient's air flow rates as shown in Figure 3.

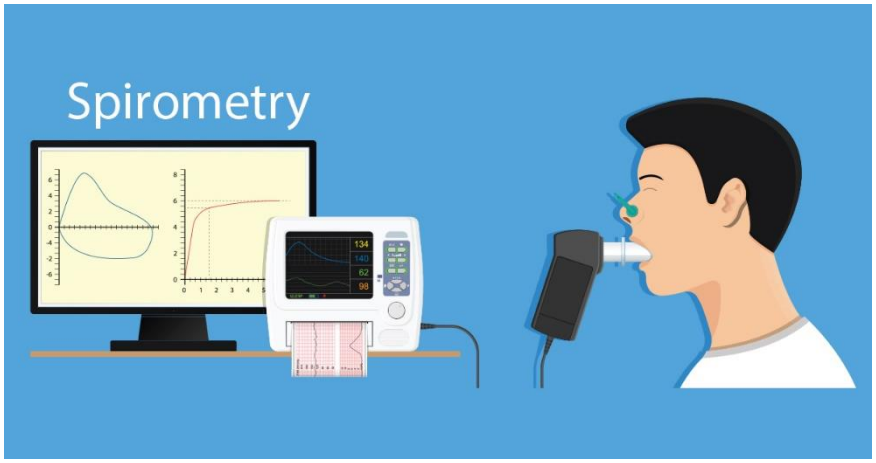

Figure 3: Spirometry pulmonary function test. Patient takes a deep breath and forcefully expels the air as fast as possible into a mouthpiece. The monitor records the amount and rate of airflow.[15]

The ratio of the forced expiratory volume in one second (FEV1) and the forced vital capacity (FVC) is then calculated (FEV1/FVC) to identify any pulmonary obstruction or restriction (Figure 4).[14] These metrics, however, provide only a *global*

measure of lung ventilation, which limits their ability to identify functional defects at the *regional* level.

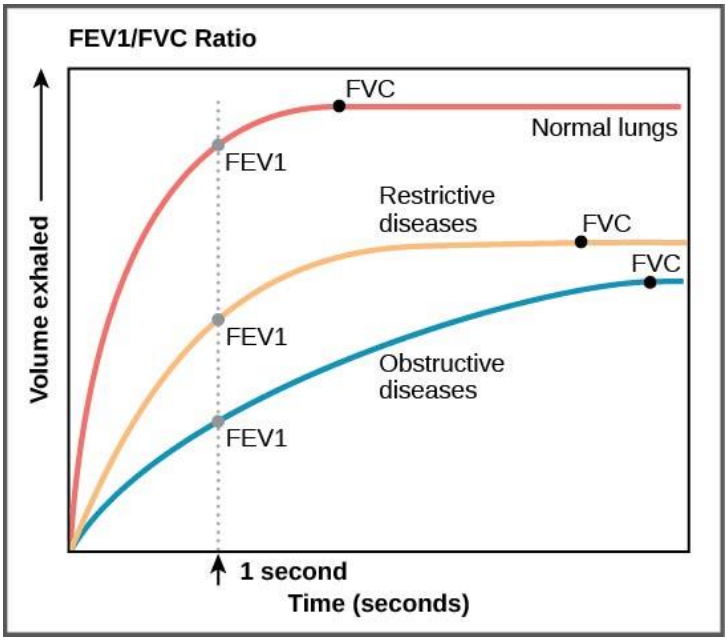

Figure 4: Spirometry flow volume curves. Results from a spirometry test, demonstrating examples of normal lung function (red curve) as well as restrictive and obstructive disease cases (yellow and blue curves, respectively).[16]

1.2.2.2 Lung Function Mapping Techniques

In an effort to evaluate lung function at the regional or local level, several techniques and modalities have been investigated. Some of these include nuclear medicine scans in which a tracer gas is used to measure lung perfusion, lung ventilation, or a combination of both of these functional metrics (commonly referred to as a V/Q

scan). Single-photon emission computed tomography (SPECT) is probably the most commonly used modality to acquire ventilation-perfusion scans, in which a tracer is inhaled to measure the airflow in the lungs (ventilation) and a tracer is also injected to measure the blood flow in the lungs (perfusion). These scans allow for visualization of the tracer's distribution throughout the lungs and are used to diagnose or identify lung diseases such as pulmonary embolism, obstruction and other relevant pathologies, as well as the extent and spatial distribution of these diseases.[17–21]

Another method that has been investigated to evaluate lung function at the local level is parametric response mapping (PRM). PRM utilizes image-processing or image-analysis techniques at the voxel level to evaluate computed tomography (CT) scans at inspiration and expiration in order to identify normal lung tissue, emphysema and functional small airway disease (fSAD). The voxels in the CT images are classified into the three main categories based on attenuation information; this is represented by thresholds in their corresponding Hounsfield Units (HU) at both inspiration and expiration following image registration. For instance, voxels with HU values below -950 HU in the inspiratory CT scan and below -856 HU in the expiratory CT scan are estimated to represent emphysema, above -950 HU inspiratory and below -856 HU expiratory are considered fSAD, and normal lung tissue would be comprised by all voxels above both thresholds in the inspiratory and expiratory CT images. Therefore, PRM can be visualized as a lung color map in order to assess the distribution and extent

of these biomarkers to inform the diagnosis of pulmonary diseases such as COPD and monitor the disease progression pathway.[22–26]

While there are varying applications, advantages and disadvantages to these different lung imaging methods and modalities, this dissertation will focus specifically on lung ventilation as a metric to evaluate lung function. As briefly discussed, ventilation of the lungs can be imaged using several different modalities involving the inhalation of tracer gases, but also through image-processing techniques. Lung ventilation imaging methods will be further discussed in the following sections.

1.2.2.3 Lung Ventilation Imaging Techniques

Lung ventilation imaging or mapping techniques have been shown to be a promising biomarker to evaluate lung function. In contrast to spirometry, ventilation images provide a regional measure of pulmonary function. Conventional methods of lung ventilation imaging include nuclear medicine scans such as gamma camera scintigraphy, single-photon emission computed tomography (SPECT), and positron emission tomography (PET) scan after inhaling a gaseous radionuclide such as 99mTc-DTPA aeorosol for SPECT or Ga-68 aerosol (Galligas) for PET.[17,18] Furthermore, hyperpolarized (HP) gas magnetic resonance imaging (MRI) using Helium-3 or Xenon-129 as imaging contrast has also been used for lung ventilation imaging, and has been gradually recognized as a validated method in the past 20 years.[8,27,28] The hyperpolarized

gas provides a strong signal within the airspaces allowing us to have a qualitative and quantitative measure of the gas distribution throughout the lungs, see Figure 5.

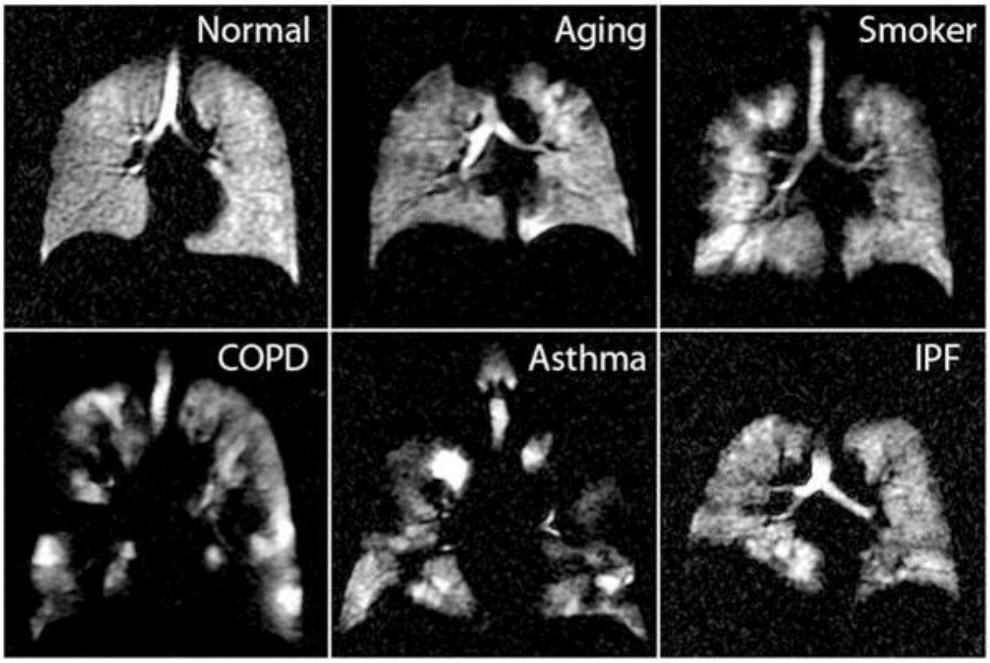

Figure 5: Hyperpolarized Gas MRI ventilation images. Ventilation images shown are from Normal, Aging, Smoker, Chronic Obstructive Pulmonary Disease (COPD), Asthma, and Idiopathic Pulmonary Fibrosis (IPF) subjects.[8]

From the images, one can see a lack of MR signal in areas within the lungs where there is low ventilation (as seen in the dark regions within the lungs) given the lower concentration of the inhaled hyperpolarized gas in those regions. As shown, normal subjects display a relatively homogeneous ventilation map, whereas patients with pulmonary diseases show much more heterogeneous lung function. These

heterogeneous distributions or regional variations in lung function allow for the identification of lung defects which are characterized by poor ventilation due to possible restriction or obstruction. Therefore, in addition to its potential applications in functional avoidance radiation therapy and radiotherapy response assessment for thoracic cancer patients, regional ventilation images would also allow us to diagnose pulmonary diseases at their earlier stages and monitor their progression.

The ventilation imaging methods described in this section all require the inhalation or injection of some type of contrast agent to image lung function (Galligas, Helium-3, Xenon-129, etc). Recently, a new method has been proposed in which a surrogate of lung ventilation is calculated based on the relative lung volume changes between respiratory phases and requires no imaging contrast. It is typically calculated through deformable image registration (DIR) of the end-of-inhalation (EOI) and end-of-exhalation (EOE) anatomical images and will be described in detail in the following chapter.

2. Specific Aims

2.1 Gap and Overall Objectives

DIR-based ventilation imaging is advantageous in its high image resolutions and simpler imaging procedures with no need for imaging contrast, making deformation-based ventilation methods a more feasible option for implementation into the clinical workflow. Additionally, DIR-based ventilation methods could potentially utilize patient images already being acquired as part of the RT treatment workflow. However, current DIR-based lung ventilation mapping techniques have been largely hampered due to two major deficiencies: 1) current DIR algorithms are morphologically based, lacking of sufficient physiological realism and thus resulting in erroneous calculations of lung ventilation; and 2) there are insufficient validation studies of the DIR-based lung ventilation calculation against a clinical ground truth, as well as large uncertainties and variations among different DIR algorithms. The *long-term goal* of this proposal is to develop the necessary tools and metrics for validation and testing of DIR-based lung ventilation mapping techniques to contribute to their clinical implementation in advanced radiotherapy of lung cancer and diagnosis of obstructive pulmonary diseases. The *objective* of the proposed research is to develop digital thoracic phantoms from physiologically-plausible lung motion models as a valuable tool for validation of DIR algorithms, and evaluate deformation-based lung ventilation mapping techniques against reference HP gas MRI ventilation images.

The goals and objectives described in this proposal will be achieved through 3 Specific Aims which are outlined in this section, and summarized in Figure 9.

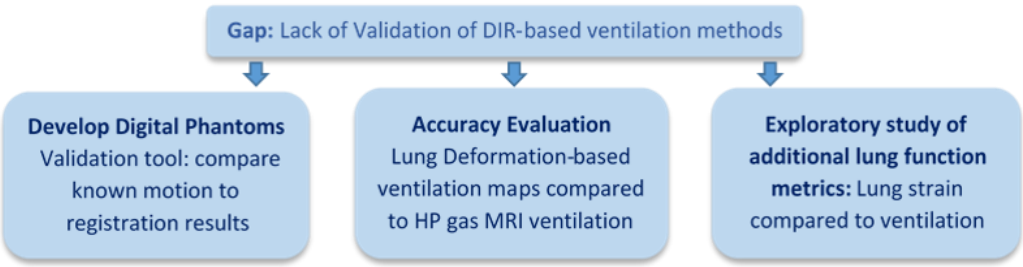

Figure 6: Diagram describing the overall study approaches to achieve the proposed goals and objectives.

2.2 Aims

Aim 1: To develop digital thoracic phantoms based on physiological modeling of respiratory motion from HP gas tagging MRI.

The purpose of this aim is to develop physiologically-plausible digital thoracic phantoms by modeling the respiratory motion of the lung from DVFs based on a combination of HP gas tagging MRI technique and proton MRI data. The respiratory motion models developed under this proposal will be a valuable tool for validation of DIR algorithms.

Aim 2: To investigate the differences between HP gas Tagging-based, DIR-based, and HP gas MRI ventilation maps.

The purpose of this aim is to evaluate the accuracy of DIR-based and tagging-based ventilation maps. The goal is to spatially compare the DIR-based ventilation maps to hyperpolarized (HP) gas tagging-based ventilation maps which are computed from ground-truth lung motion from a novel HP gas tagging MRI technique, as well as to the ground-truth ventilation maps from the HP gas MRI.

Aim 3: To evaluate and compare the sensitivity to deformation changes of ventilation and strain as lung functionality metrics.

This aim investigates lung strain as an additional metric to assess lung function. This study utilizes physiologically-based respiratory motion models to assess the sensitivity of lung strain and lung ventilation by introducing a number of modifications to the DVF, generating new lung functional maps, and investigating how much each of these lung functional metrics are affected. The deformation fields utilized for this study are tagging-based DVFs obtained from a HP gas tagging MRI technique.

3. Methods and Materials

3.1 Deformation-based ventilation mapping

3.1.1 Deformable Image Registration

Image registration is the process of finding the geometrical transformation of an image to establish a spatial correspondence with another one. There are two main types of image registration: rigid image registration (RIR) and deformable image registration (DIR). The key difference between the two is that, in rigid registration, the geometrical transformation is uniform for all pixels or voxels. Therefore, the pixel-to-pixel relationships remain unchanged before and after the geometrical transformation, which is not the case for DIR.[29] Deformable Image Registration has more degrees of freedom and manages distortions between the two images. This is particularly useful in radiation therapy for dose accumulation calculations in order to estimate delivered dose during the course of treatment where anatomical structure changes might be expected in between fractions. This may be due to a shrinking tumor, organ shape variations, or patient weight loss to name a few examples.[29]

In an image registration, one set of images is considered to be "fixed" F(x) while the other is considered to be the "moving" image set M(x'). The registration algorithm finds the best transform T(x') to minimize differences between the two image sets F(x) and M(T(x')) (the fixed and the deformed moving image) through an iterative process. The "transform is the sum of the local position vector in the moving image x', and the

displacement vector, u(x′).”[29] Equation 1 expresses the ideal relationship between the two images:[29]

$$F(x) = M\big(T(x')\big) = M\big(x' + u(x')\big) \quad (1)$$

Figures 7 and 8 from the manuscript *Deformable image registration in radiation therapy*,[29] , describe the image registration process:

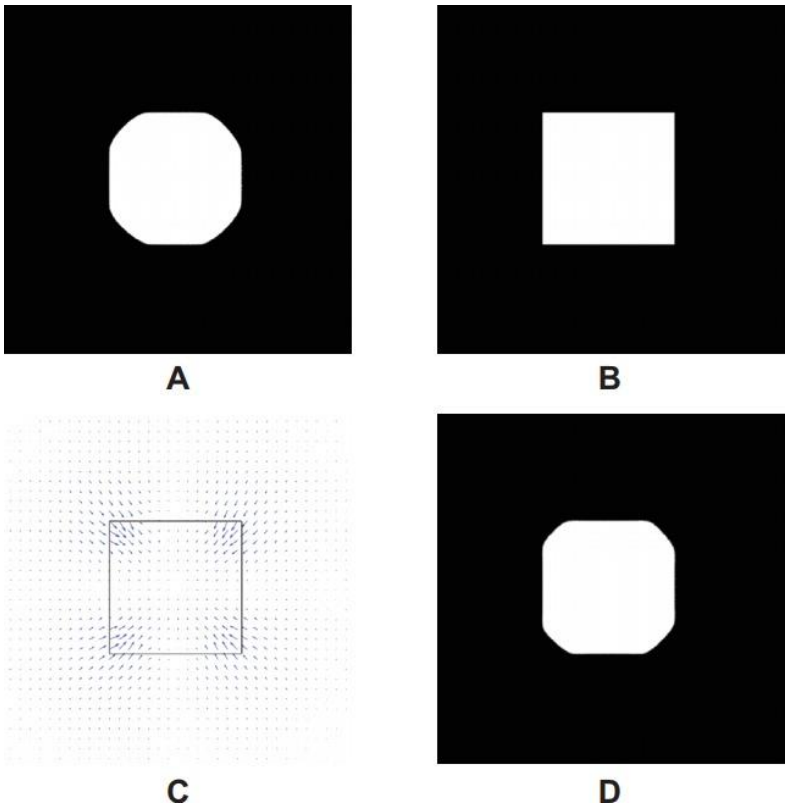

Figure 7: Deformable image registration of fixed image (A) and moving image (B). The DVF (C) that describes the deformation is displayed, the blue arrows represent the magnitude and direction of the vectors. The resulting deformed image is shown (D).[29]

The goal is for the deformation field or DVF to accurately describe how the pixels or voxels in the moving image have been displaced with respect to their initial positions in the fixed image and establish a point-to-point correspondence.

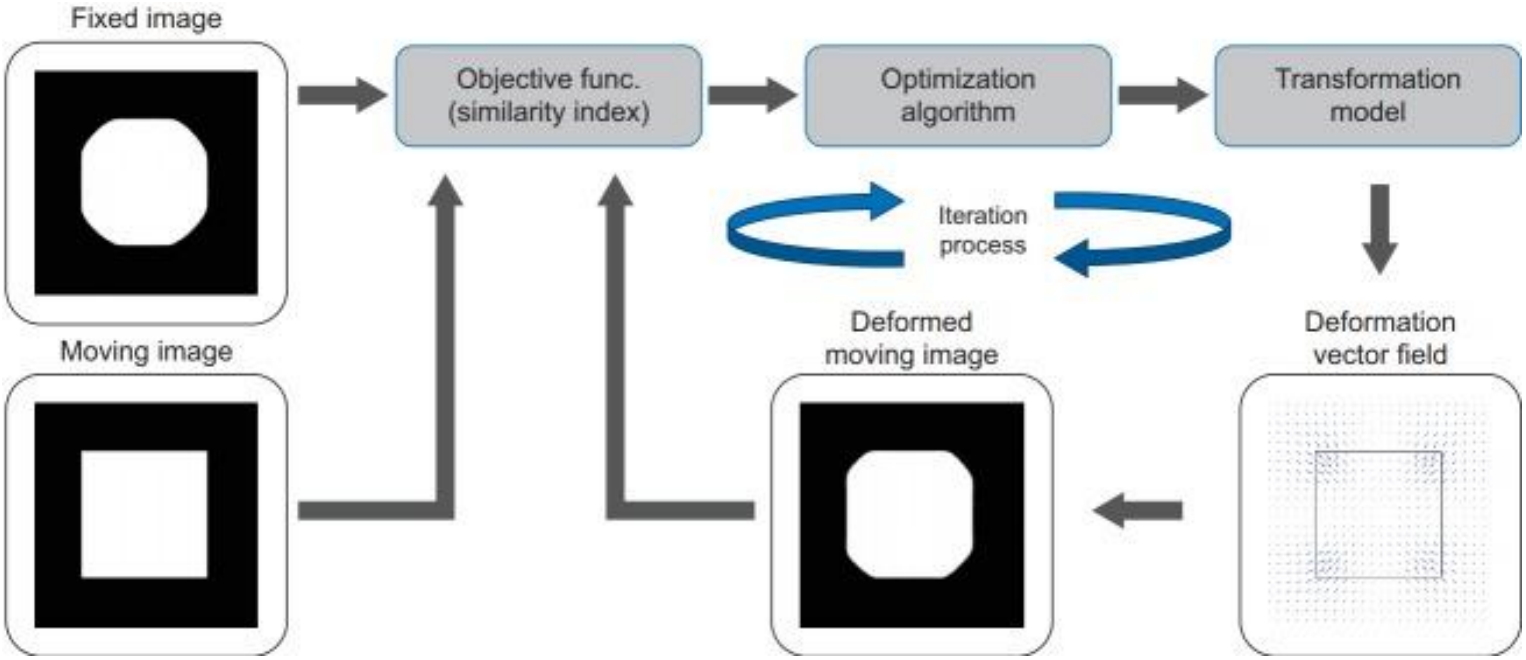

Figure 8: Deformable image registration process.[29]

The optimization algorithm tries to find the transformation that maximizes the similarity index between the fixed and moving images through an iterative process. Depending on the DIR algorithm, different similarity indices might be used such as mutual information (MI), cross correlation (CC), mean square differences (MSD), etc. In this iterative process, the algorithm changes the DVF that deforms the moving image, and recalculates the similarity index between the deformed moving image and the fixed image until the differences between the two sets are minimized and the function has met its target.

In conclusion, the deformation of a body can be described by a displacement vector field. For this study, the extraction of the DVF from a deformable image registration algorithm becomes particularly useful in order to mathematically model the deformation of the lungs as they expand and contract between different respiratory phases in a respiratory cycle, such as EOI and EOE.

3.1.2 DIR-based ventilation

By performing a DIR on two anatomical image sets from two different respiratory phases, a 3D DVF of the lungs can be obtained that mathematically describes the lung tissue deformation on a voxel-by-voxel basis. Lung ventilation can then be quantified as the regional relative lung volume change between the two respiratory phases, and computed from the 3D lung DVF as described in Figure 9.[30–36] There are two main methods that have been frequently used in the literature; one is based on the

Jacobian Determinant of the DVF, and the second one is a Hounsfield Unit (HU)-based calculation when utilizing computed tomography (CT) images.[35,37–40] This dissertation will focus on the Jacobian method, but will include a brief explanation on both methods for completeness.

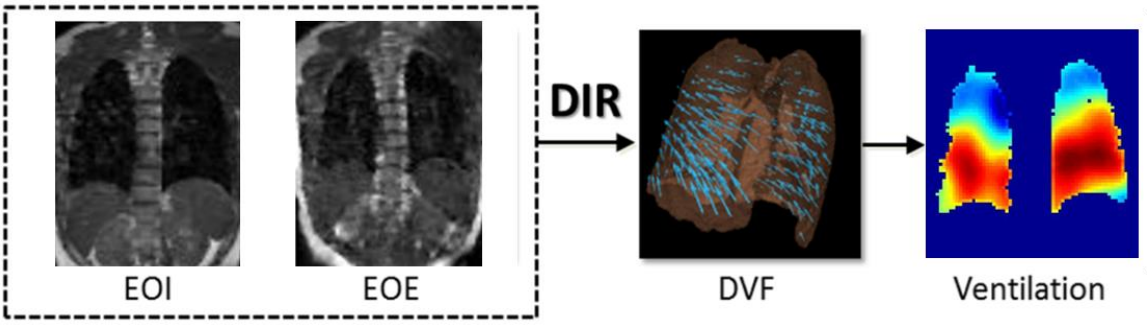

Figure 9: DIR-Based Ventilation Workflow. Anatomical images of the lungs from two respiratory phases (typically EOI and EOE) are deformably registered, the DVF is extracted from which a ventilation map is calculated.

It is important to emphasize that DIR-based ventilation calculation methods are based on the assumption that local volume changes within the lungs are a feasible surrogate of lung ventilation (i.e. airflow).[38]

The regional ventilation at a certain voxel or position $V(x, y, z)$ would then equal the relative change in volume from one respiratory phase to another:

$$V(x,y,z) = \frac{V_1(x,y,z) - V_2(x,y,z)}{V_2(x,y,z)} = \frac{V_1(x,y,z)}{V_2(x,y,z)} - 1 \quad (2)$$

DIR-ventilation studies in the literature have used anatomical CT images to calculate ventilation from the DVF. The CT images utilized in these ventilation studies have mainly utilized breath-hold CT or 4DCT image sets from either human or animal subjects.[18,35–41] The focus has been on utilizing images already acquired during RT patient simulation and treatment planning. Therefore, ideally, once these methods become fully validated, functional information from the DIR-based ventilation maps could be easily implemented into the RT treatment workflow for functional avoidance treatment planning and radiotherapy response assessment applications without having the patient undergo any additional imaging.

3.1.2.1 Jacobian Determinant

The Jacobian Determinant is a mathematical method used to calculate local volume changes. The "Jacobian", as it is often referred to in the literature, represents changes in differential volume from the transformation of coordinates.

In vector calculus, the Jacobian Matrix is a matrix composed of the first-order partial derivative for a vector-valued function; it represents the differential of the vector-function. The determinant of this matrix is called the Jacobian Determinant.

The Jacobian Determinant or Jacobian provides information about the local behavior of the function. Its absolute value gives the magnification factor of the function (the factor by which the function expands or contracts volumes locally). Therefore, the result from this calculation equals the magnification factor of each voxel under the transformation, and as such, a Jacobian factor of 1 represents no volume change, while a factor greater or smaller than 1 represents a volume increase or decrease, respectively.

For a given DVF $u(x,y,z)$ that transforms the volume of the EOI lung image V_1 to V_2 from the EOE image, the Jacobian of the transformation $J(u(x,y,z))$ which equals the magnification factor is given by the following mathematical expression, where I is the Identity matrix:

$$J(u(x,y,z)) = \left| I + \begin{pmatrix} \frac{\partial u_x(x,y,z)}{\partial x} & \frac{\partial u_x(x,y,z)}{\partial y} & \frac{\partial u_x(x,y,z)}{\partial z} \\ \frac{\partial u_y(x,y,z)}{\partial x} & \frac{\partial u_y(x,y,z)}{\partial y} & \frac{\partial u_y(x,y,z)}{\partial z} \\ \frac{\partial u_z(x,y,z)}{\partial x} & \frac{\partial u_z(x,y,z)}{\partial y} & \frac{\partial u_z(x,y,z)}{\partial z} \end{pmatrix} \right| \quad (3)$$

The Jacobian is a simple mathematical method that enables us to calculate local volume changes in the lungs during respiration and has been one of the key methods utilized in the field of DIR lung ventilation mapping. The number of studies that have incorporated this calculation method has been growing in the past few years in an effort to validate it as a feasible method for the calculation of a ventilation surrogate.[35,36]

3.1.2.2 HU-Based CT Ventilation

Hounsfield Units (HU), also known as CT numbers, are a dimensionless unit to quantitatively measure radiodensity in CT scans. CT images are reconstructed to produce grayscale images based on the attenuation of radiation in tissue, which is proportional to the tissue's physical density. In the HU unit scale, water is assigned a value of 0 HU, and air is defined as -1000 HU. The HU value of a voxel with a linear attenuation coefficient μ is:

$$HU = 1000 * \frac{\mu - \mu_{water}}{\mu_{water} - \mu_{air}} \quad (4)$$

HU-Based CT ventilation methods are based on calculating volume changes within the lungs from density variations in the CT images' which are described by the Hounsfield units.[38,39,42] This method assumes that the fraction of air F_{air} in a region of the CT is given by:

$$F_{air} = -\frac{HU}{1000} \quad (5)$$

Therefore, if the local volume change ΔV due in inhalation is given by:

$$\Delta V = V_{in} - V_{ex} \quad (6)$$

where V_{in} is the volume at inhalation and V_{ex} is the volume at exhalation, then the local fractional volume change $\frac{\Delta V}{V_{ex}}$ can be calculated through:

$$\frac{\Delta V}{V_{ex}} = \frac{F_2 - F_1}{F_1(1 - F_2)} = \frac{F_{ex} - F_{in}}{F_{ex}(1 - F_{in})} \quad (7)$$

Which in terms of HU becomes:

$$\frac{\Delta V}{V_{ex}} = 1000 \frac{HU_{in} - HU_{ex}}{HU_{ex}(1000 + HU_{in})} \quad (8)$$

In this method, the DIR is utilized to establish the point-to-point correspondence between the voxels of the inhalation and exhalation CT images, and the volume change is calculated from the density change information. Both the Jacobian and this HU-based ventilation calculation method estimate ventilation based on local volume changes. Given that the HU-method utilizes Hounsfield Unit information, it is of course only applicable to ventilation mapping techniques using CT images, while the Jacobian method could be more versatile in terms of imaging modality, given that it only requires the displacement vector field which can be obtained from the DIR of a pair of anatomical images regardless of the imaging modality.

3.1.2.3 Advantages and Limitations

Compared to other methods, the DIR-based lung ventilation method is advantageous in its higher image resolutions compared to nuclear medicine scans and

simpler imaging procedure compared to scans requiring the injection or inhalation of contrast agents, making it more promising for clinical applications.

However, although a number of studies have demonstrated promising results for the DIR-based lung ventilation method, two major obstacles have largely hampered the clinical application of this method: 1) current DIR algorithms are morphologically based, lacking of sufficient physiological realism and thus resulting in erroneous calculations of lung ventilation; and 2) there is a lack of validation of the DIR-based lung ventilation calculation against clinical ground truth, as well as large uncertainties and variations among different DIR algorithms.

3.2 Hybrid Hyperpolarized Gas MRI Technique

This study investigates a unique dataset which includes three types of MR images acquired using a novel hybrid technique in a single breath-hold maneuver: a HP He-3 ventilation image (v-MRI), a pair of proton MR images at EOI and EOE (p-MRI), and a pair of HP He-3 tagging images at EOI and EOE (t-MRI), for a total of 5 images per subject as shown in Figure 10.[43,44]

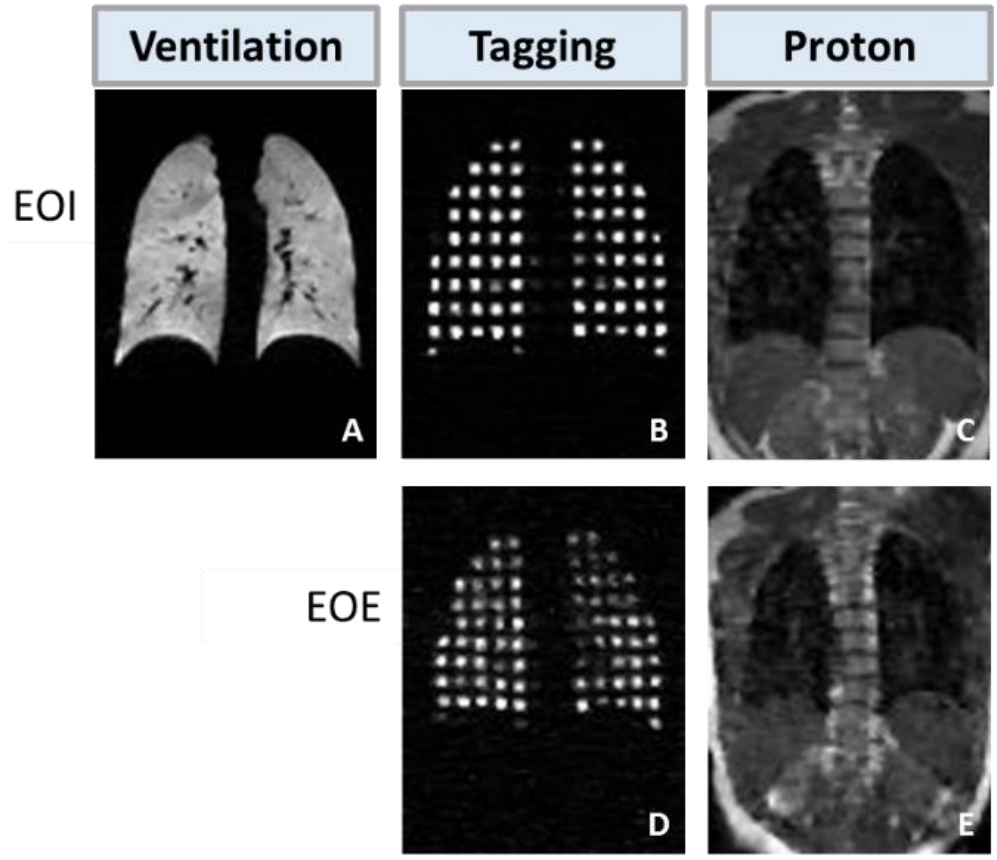

Figure 10: Five images acquired for each subject. Images include a ventilation MR image at EOI (A), a pair of tagging MR images at EOI and EOE (B & D) and a pair of proton MR images at EOI and EOE (C & E).

3.2.1 Image Acquisition and Parameters

In this section, the technical aspects regarding the MR image acquisition and parameters will be described. Images from four healthy subjects were utilized in this study under an IRB-approved protocol. Subjects were never-smokers and had no history

of lung disease. The images were acquired at the University of Virginia in collaboration with their radiology department.

The subjects underwent MR imaging on a 1.5 Tesla whole-body scanner (Avanto, Siemens Healthineers, Malvern, PA). A rigid, elliptically shaped, linearly polarized, transmit/receive radiofrequency (RF) coil tuned to the Helium-3 (He-3) resonance frequency (RAPID Biomedical International, Columbus, OH) was placed on the scanner table, and the subject was positioned supine in the scanner with the RF coil encircling the torso. This RF coil contains passive circuitry that blocks it from resonating at the proton MR frequency, permitting the scanner body coil to acquire proton images of the subject while the He-3 RF coil is in place.

Proton, He-3 ventilation, and He-3 tagged images were acquired using a balanced steady-state free precession (SSFP) pulse sequence with nonselective excitation RF pulse and an undersampled 3D Cartesian k-space trajectory.[45,46] Images were reconstructed from undersampled data using previously described compressed-sensing techniques.[46]

Pulse sequence parameters for proton images included: TR/TE = 1.56/0.78 ms, flip angle = 25°, bandwidth = 1700 Hz/pixel, field-of-view = 408 × 512 × 240 mm^3, fully sampled k-space matrix = 104 × 128 × 60, voxel size = 4 × 4 × 4 mm^3, undersampling factor = 3, acquisition time per image = 3.4 s.

Pulse sequence parameters for He-3 images (ventilation and tagged) included: TR/TE = 1.84/0.92 ms, flip angle = 9°, bandwidth = 1440 Hz/pixel, field-of-view = 277 × 370 × 198 mm^3, fully sampled k-space matrix = 84 × 112 × 60, voxel size = 3.3 × 3.3 × 3.3 mm^3, with the exception of Subject 1 whose images had a voxel size of 4 x 4 x 4 mm3, undersampling factor = 3 (vent) or 8 (tagged), acquisition time per image = 3.1 s (vent) or 1.1 s (tagged).

Helium-3 gas was polarized to ~60% using a homebuilt device.[47] A disposable inhalation apparatus was constructed for each subject, consisting of two 0.75 L Tedlar bags (Jensen Inert Products, Coral Springs, FL) each connected by 3/8" tubing to a tee connector. A tubing clamp was placed around each of the tubes. One of the bags was filled with 600 ml of polarized He-3 gas and the other was filled with 150 ml of medical grade nitrogen, and both tubes were clamped shut before connecting them to the tee. A one-way valve was inserted in the tee connection leading to the helium-3 bag, and a mouthpiece was connected to the third end of the tee connector (Amici Inc., Spring City, PA). Prior to imaging, the subject was instructed to take in a normal breath and then "sigh" to exhale to residual capacity. Then the mouthpiece was placed in the subject's mouth and the subject was instructed to begin inhaling. The study nurse opened the two bag valves in succession: first He-3 and then nitrogen. The nitrogen valve was opened second to wash inhaled helium-3 out of the large airways and into the parenchymal airspaces.

All 5 images (proton EOI, ventilation, tagged EOI, tagged EOE, and proton EOE) were acquired during the same breath-hold maneuver. Immediately following helium-3/nitrogen inhalation as described above, the proton EOI and He-3 ventilation images were acquired at breath hold, then the tag pattern was applied and the tagged EOI image was acquired. At this point the pulse sequence execution paused for 2.5 seconds, and the subject quickly exhaled a volume of 0.75 L through the mouthpiece and into the bag that previously held nitrogen. (The one-way valve prevented exhaled air from re-entering the helium-3 bag.) Then the pulse sequence resumed, and the tagged EOE and proton EOE images were acquired at breath hold. Figure 11 describes the hybrid MR image acquisition process.

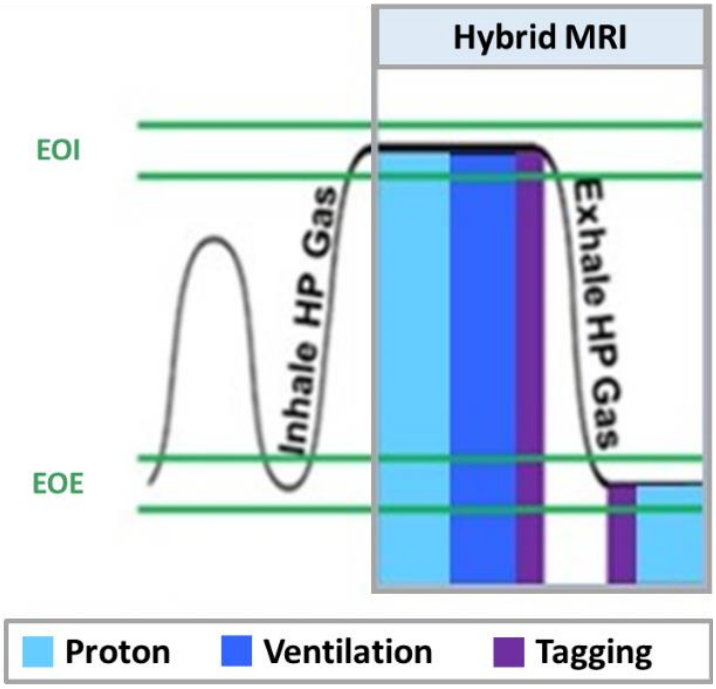

Figure 11: Hybrid image acquisition. The subject inhales the HP gas followed by the acquisition of the proton, ventilation and tagging images at EOI, then the subject exhales the HP gas and the tagging and proton images are acquired at EOE.

4. Digital Thoracic Phantom

4.1 Background on DIR validation tools

One of the limitations of the use of DIR in radiation therapy are the uncertainties associated to different DIR algorithms.[48] There can be large variations on the DVF output from different DIR algorithms given that they may use varying mathematical methods, similarity metrics, landmarks, interpolation methods, etc. Therefore, there have been efforts to validate DIR which have consisted on three main approaches: anatomical landmarks, physical phantoms, and digital phantoms.[29]

4.1.1 Anatomical Landmarks

Anatomical landmarks are most frequently used to estimate the accuracy of a DIR. However, it is difficult to measure the accuracy of registration where the landmarks do not exist and, in DIR, it is important to be able to measure the accuracy of the registration at the local level. Landmarks are usually not available throughout the entire image, and it is difficult to identify landmarks in certain organs. The use of injected or implanted markers or seeds has also been investigated, but the introduction of these can certainly alter the registration results, especially for intensity-based DIR algorithms.

4.1.2 Physical Phantoms

Physical phantoms have also been used to evaluate DIR. The phantom is deformed to a known deformation which is then used as reference to evaluate the DIR-

generated DVF. Physical phantoms commonly have embedded markers from which the ground-truth deformation can be measured. The limitations of physical phantoms are that they lack physiological realism and commonly have insufficient anatomical structures.

4.1.3 Digital Phantoms

In digital phantoms, there is usually an image set used as reference, and another image that is synthesized from a pre-defined DVF and considered the deformed image set. The images are then registered through a DIR algorithm, and the resulting DVF is compared to the pre-defined DVF which is considered the "ground truth" deformation. This method provides the densest DVF information, but similar to one of the limitations of the physical phantoms, the pre-defined DVF might lack physical or physiological realism.

The use of digital phantoms has been proposed by the American Association of Physicists in Medicine Task Group Report 132 (AAPM's TG-132) *"Use of Image Registration and Data Fusion Algorithms and Techniques in Radiotherapy Treatment Planning"* as a DIR validation tool and testing standardization. In this dissertation, we will focus on investigating the digital phantom validation method. However, the limitations regarding the lack of physiological realism will be addressed by creating a physiologically-plausible respiratory motion model.

4.2 Respiratory Motion Modeling

In order to create a physiologically plausible lung motion model, we used the novel HP gas tagging MRI technique. The HP ^{3}He tagging images are acquired using the described hybrid MR image acquisition technique in which, after the inhalation of the HP gas, a non-imaging pulse sequence saturates the magnetization in a 3D grid pattern as seen in the tagging images shown in Figure 12. As explained in Chapter 2, the change in configuration or deformation of a body can be described by a vector field of all displacement vectors. The 'tag' pattern is imaged both at EOI and EOE, and the deformation of this pattern is used to calculate lung motion as described by the displacement vector field (DVF).[44]

The 3D tagged grid pattern in the tagging MR images (t-MRI) contains, approximately, 400-500 uniformly distributed grid elements with isotropic tag spacing of 11mm and a tag width of 9mm as shown in Figure 13. Diffusion of the hyperpolarized gas utilized as imaging contrast and the speed of the image acquisition limit the tag spacing and tag width in order to avoid the tag elements from "meshing" together and becoming undiscernible in the exhalation image. Advances in the image acquisition technique will continue to allow an increase in the number of grid elements, in order to create denser deformation models.

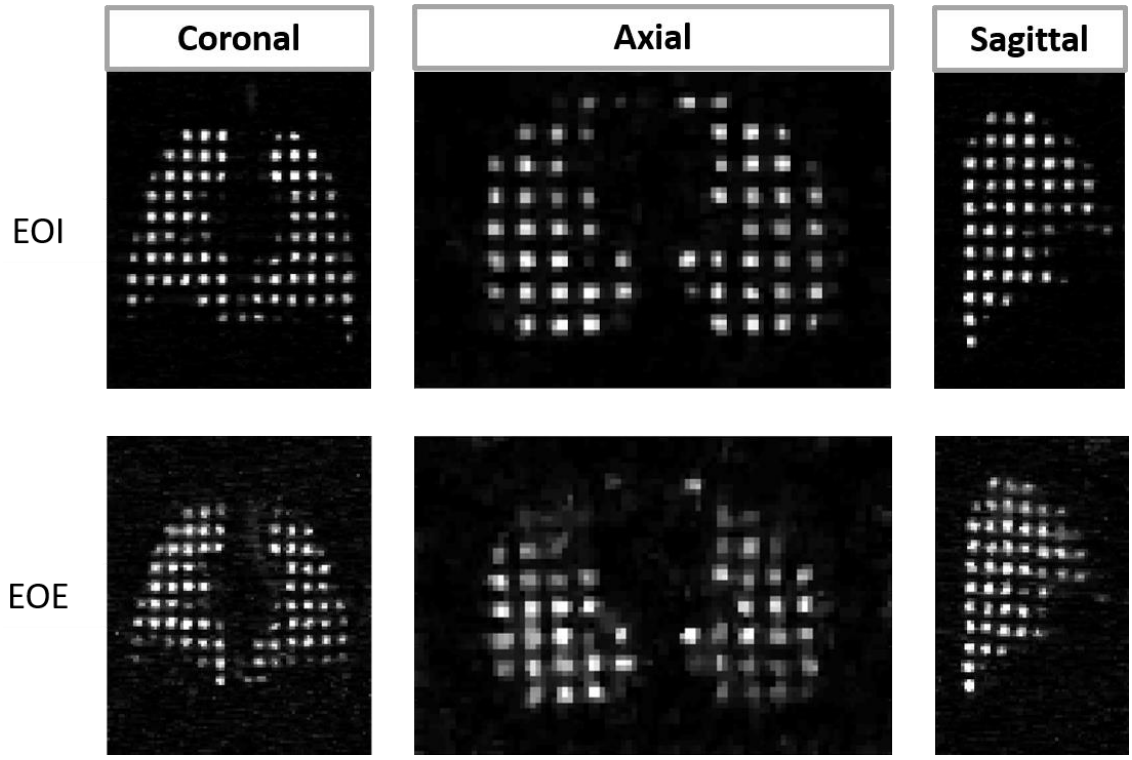

Figure 12: HP MR Tagging Images in Coronal, Axial and Sagittal planes during EOI and EOE phases.

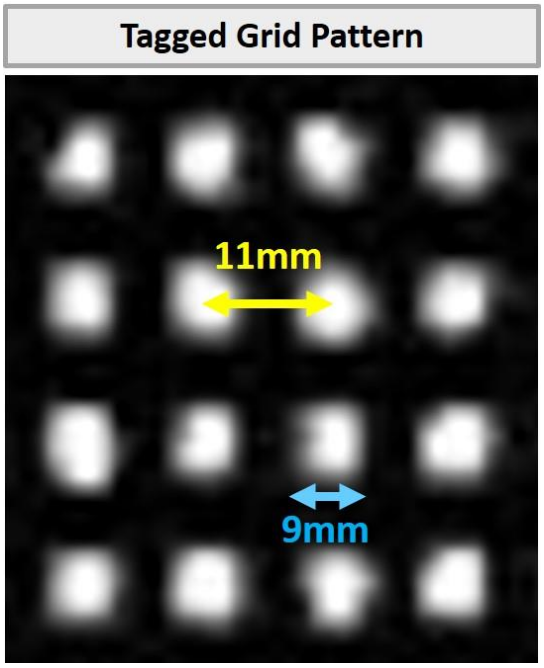

Figure 13: Tagged grid pattern in the tagging MR images (at EOI) with tag spacing (yellow) and tag width (blue) shown.

The tagging-based lung deformation was manually measured for 4 healthy subjects. The EOI and EOE t-MRIs were imported into the Eclipse treatment planning system (Varian Medical Systems, Palo Alto, CA) and the displacement of the tagging grid elements was measured by manually tracking their center of mass from EOI to EOE. The sparse tagging-based DVF (t-DVF) was obtained by calculating the difference in each element's coordinates between the two respiratory phases.[44] The tagged elements are essentially ~500 evenly distributed landmarks throughout the entire lung area. Therefore, the displacement vector field calculated by tracking their motion between the

two respiratory phases provided us with a true lung deformation model which is physiologically-based, see Figure 14.

4.2.1 Results

Once the t-DVF was measured for all 4 subjects, the mean amplitude of the t-DVF describing the lung motion from EOI to EOE in millimeters (mm) was calculated as seen in Table 1. The mean displacements ranged from 11.8 mm to 18.7 mm, with Subject 2 exhibiting the largest mean displacement and Subject 3 exhibiting the smallest. The standard deviation among subjects was 2.9 mm.

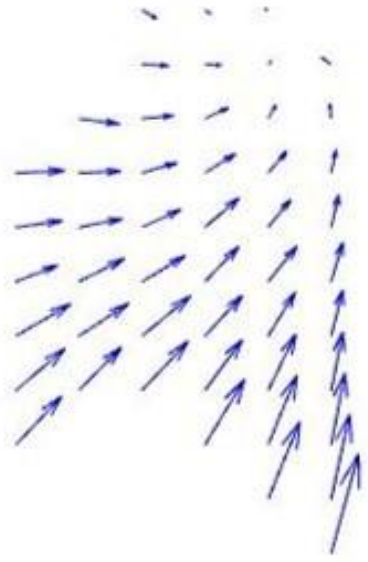

Figure 14: Visualization of t-DVF in sagittal plane describing lung deformation from EOI to EOE.

Table 1: Mean Tagging-based displacement magnitudes (in mm) for 4 healthy subjects. The t-DVF was measured from manually tracking the motion of the tagging elements from EOI to EOE. The number of tagged elements for each subject is also shown.

	Mean Displacement (mm)	Number of Tagged Elements
	Tagging	
Subject 1	16.4	460
Subject 2	18.7	396
Subject 3	11.8	494
Subject 4	14.7	485
Average	**15.4**	
Std. Deviation	**2.9**	

4.3 DVF Evaluation

The tagging-based displacement vector fields measured from the displacement of the tagged grids were used as reference deformation models to evaluate the accuracy of DIR-based DVFs (d-DVF).[44] The t-DVF provides a reference lung deformation model which provides a novel evaluation tool.

Deformable image registration was performed on the proton MR images (p-MRI) from EOE to EOI using the Deformable Multi-Pass algorithm from the commercially-available software Velocity AI (Varian Medical Systems, Palo Alto, CA). Velocity AI is a B-spline registration algorithm which uses Mutual Information (MI) as its similarity

metric. The d-DVF was extracted which described the deformation of the lungs between the two respiratory phases.

Both the tagging-based DVF and the DIR-based DVF (t-DVF and d-DVF) within the lungs were compared by calculating the difference in vector magnitudes between the two (||DVF||), as well as the differences in their corresponding vector components (Dx, Dy, Dz).

4.3.1 Results

The t-DVF and d-DVF were compared by calculating the magnitude differences in their DVFs. The differences were calculated between the sparse t-DVF and the d-DVF vectors at the particular voxel locations that matched the tagged grid elements, in order to avoid introducing uncertainties from any kind of interpolation of the sparse t-DVF. Therefore, the coordinates from each tagged element were used to determine the corresponding voxel positions, and ensure a point-to-point spatial correspondence between the t-DVF and the d-DVF at those locations, especially in the cases of Subjects 2,3,4 which had different p-MRI and t-MRI image resolutions.

The mean absolute DVF differences were found to be 8.2 mm [8.1 mm in the anterior-posterior (AP) component, 8.2 mm in the lateral (LAT), and 14.4 mm in the superior-inferior (SI) component] for Subject 1; 7.5 mm [4.8 mm (AP), 4.9 mm (LAT), 6.5 mm (SI)] for Subject 2; 5.6 mm [4.9 mm (AP), 5.4 mm (LAT), 8.2 mm (SI)] for Subject 3;

8.8 mm [4.5 mm (AP), 6.9 mm (LAT), 9.8 mm (SI)] for Subject 4. These results are summarized in Tables 2 and 3.

Table 2: Mean displacements (in mm) of Tagging-based and DIR-based DVFs.

	Mean Displacement (mm)	
	Tagging	**DIR**
Subject 1	16.4	13.7
Subject 2	18.7	15.1
Subject 3	11.8	7.8
Subject 4	14.7	6.8
Average	**15.4**	**10.9**
Std. Deviation	**2.9**	**4.1**

Table 3: Comparison of Tagging-based and DIR-based DVFs.Showing the mean absolute DVF differences in the 3 vector components as well as in vector magnitude ||DVF||.

	DVF differences (mm)			
	AP	**LAT**	**SI**	**||DVF||**
Subject 1	8.1	8.2	14.4	8.2
Subject 2	4.8	4.9	6.5	7.5
Subject 3	4.9	5.4	8.2	5.6
Subject 4	4.5	6.9	9.8	8.8
Average	**5.6**	**6.3**	**9.7**	**7.5**
Std. Deviation	**1.7**	**1.5**	**3.4**	**1.4**

The largest differences were shown to be in the SI direction. This makes sense since the lungs exhibit the largest displacement in the superior-inferior direction as the subjects inhale/exhale. These results show that there can be significant differences in DVF when performing a DIR compared to the respiratory motion models created from the tagged elements' displacement.

4.4 Thoracic Motion Model

In order to create a model of the entire thorax, the proton MR images at EOI and EOE as well as the respiratory motion model DVF information from the tagging MR at EOI and EOE were combined. The p-MRIs at EOI and EOE were deformably registered using Velocity AI. This DIR-based DVF was utilized to model the respiratory motion *outside* the lungs. Using a lung segmentation or "mask", the vector field *within* the lungs was eliminated.

Lung masks were created using a semi-automatic image segmentation method from ITK-SNAP.[49] After indicating the region of interest (ROI), segmentation was performed using a region growing method from manually placed seeds throughout the lung region and then manually brushing out major airways, as shown in Figure 15.

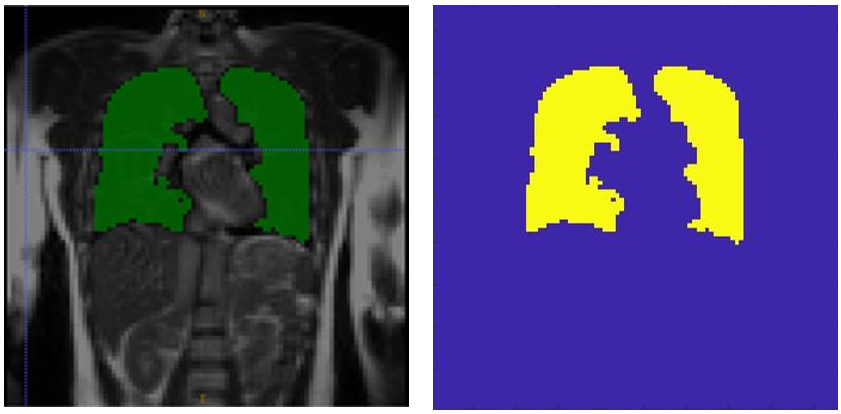

Figure 15: Lung segmentation using ITK-SNAP (left) and binary lung mask (right).

The DVF within the lungs was then replaced with the tagging-based DVF which describes the true lung motion measured by tracking the displacement of the tagged grid elements as described in Section 4.2. Due to the sparse nature of the tagging-based DVF, it was interpolated throughout the entire lung region through a combination of two MATLAB functions, "griddata" and "fillmissing", which used natural neighbor and spline interpolation algorithms to match the resolution of the DIR-based DVF.

The thoracic motion model was then created through a combination of the DIR-based DVF outside the lungs calculated from the registration of the p-MRIs, and the tagging-based DVF inside the lungs manually measured from the t-MRIs (d-DVF and t-DVF) as described in Figure 16. Therefore, even though the true motion would only be represented within the inside of the lungs, the DIR-based DVF outside of the lungs allows for the creation of a motion model of the entire thoracic area.

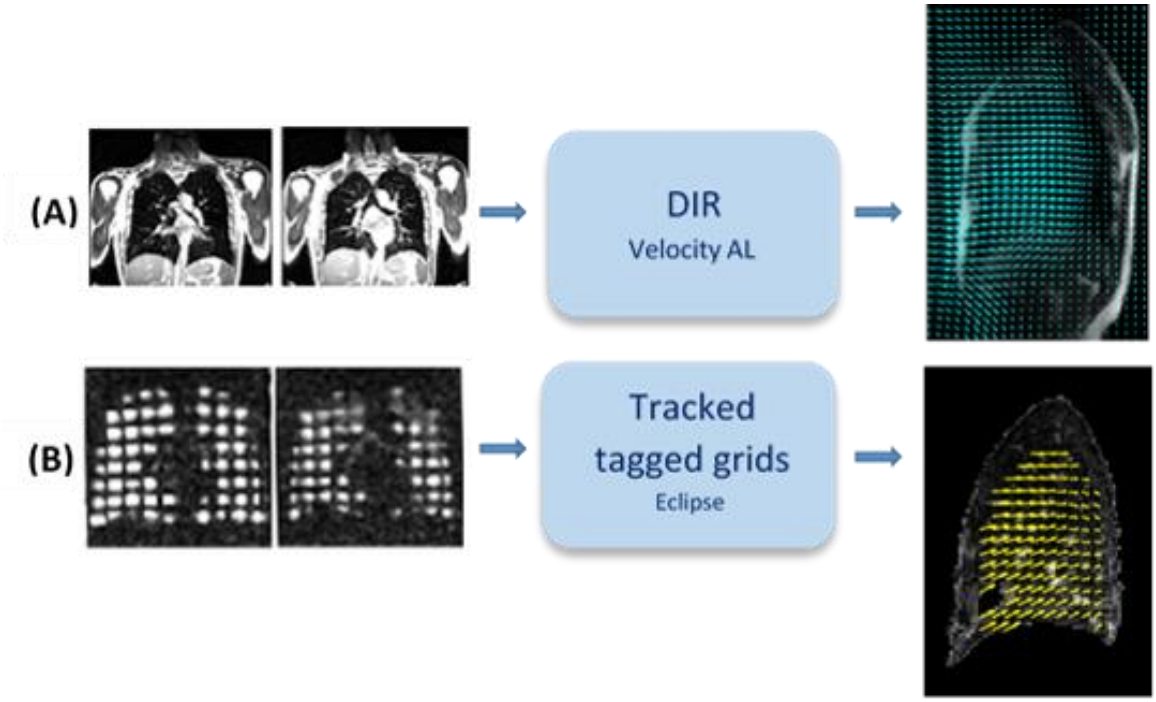

Figure 16: Workflow describing the computation of the DVFs used to create the thoracic respiratory motion model. In (A) the p-MRIs at EOI and EOE were registered through DIR to obtain the DVF of the thorax. In (B) the t-MRIs at EOI and EOE were used to track the displacement of the tagged elements to obtain the DVF within the lungs.

This thoracic motion model describes the deformation of the entire thoracic region, with the deformation field inside of the lungs being physiologically-based, unlike current thoracic models which may lack physical realism as discussed in section 4.1

5. Investigation of HP gas tagging-based, DIR-based, and HP MRI ventilation maps

5.1 Background

We have discussed throughout this dissertation, the importance and need for validating ventilation calculation methods against a ground truth or reference lung ventilation imaging modality. While there have been efforts to evaluate these methods, previous studies have certainly shown how different DIR algorithms can have a significant impact on the spatial correlation between DIR-based ventilation calculation methods and reference modalities.[35] The main focus has been on validating DIR-based ventilation methods using CT images (commonly referred to as "CT ventilation"). The reasoning behind this is that most radiation therapy patients go through CT imaging for simulation and treatment planning. The main goal is to potentially clinically implement these ventilation calculation methods into the clinical workflow by incorporating functional information into treatment planning, and therefore CT Ventilation studies are key in this regard. However, there have been important limitations in addition to the variations in DIR algorithms, such as variations in respiratory cycle and patient positioning.

Most past CT Ventilation evaluation studies have used different modalities for validation. These studies have evaluated DIR-based ventilation maps computed using end-of-inhalation and end-of-exhalation CT or 4DCT images, with more established

ventilation imaging techniques including gamma camera scintigraphy and positron emission tomography scan after inhaling a gaseous radionuclide, as well as Hyperpolarized Gas Magnetic Resonance Imaging (MRI) using Helium-3 and Xenon-129 as imaging contrast, as it was covered in the Introduction section.[35,36] However, current DIR-based lung ventilation mapping techniques have been largely hampered not only due to the lack of validation of the DIR-based lung ventilation calculation against a clinical ground truth, but also because of the large uncertainties associated with the different DIR-algorithms, and the fact that, for the acquisition of reference or 'ground-truth' ventilation images, the subjects or patients are imaged at a different time and using different scanners and modalities. This makes it difficult to reproduce patient positioning, and to account for the variations in respiratory cycle during the two separate image acquisitions. This can of course greatly affect the spatial correlations between reference and DIR-based ventilation images.

5.2 Purpose

The purpose of this study was to investigate a deformable image registration - based lung ventilation imaging technique using proton MR images by evaluating its correlation with hyperpolarized Helium-3 gas ventilation MRI reference images which provide a ground-truth measure of lung ventilation. Correlation between the reference ventilation images and ventilation maps computed from HP gas tagging MRIs, which provide ground-truth lung deformation, was also investigated.

5.3 Innovation

This study is innovative on several levels. First, all 3 ventilation images/maps in this evaluation utilize data from the same modality: MRI. Second, and very importantly, all images/data used in our evaluation are acquired during one same breath hold in a 1.5T Siemens MR scanner (refer back to Figures 10 and 11). This eliminates the uncertainties associated with reproducibility of the respiratory cycle, patient positioning, and finding the spatial correspondence between the ventilation maps being evaluated. Lastly, the novel HP Gas Tagging MRI technique provides a ground-truth deformation field consisting of ~500 tagged grids, essentially 'landmarks', which are evenly distributed throughout the entire lung region. By calculating ventilation using this true lung motion model, it gives us an important insight on the accuracy of deformation-based ventilation (surrogate) calculation methods that is not affected by the uncertainties of DIR algorithms.

5.4 Methods and Materials

5.4.1 Reference Helium-3 Ventilation Images

The reference or ground truth ventilation images used in this evaluation study were the hyperpolarized gas (He-3) ventilation images acquired in the hybrid MR image acquisition described in Chapter 4. Recall that, once inhaled, hyperpolarized gas provides a strong MRI signal in the lung airspaces, enabling a voxel-by-voxel imaging of

gas concentration used to measure lung ventilation as seen in Figure 17. The He-3 MR ventilation images have a resolution of 4 mm x 4mm x 4mm voxels.

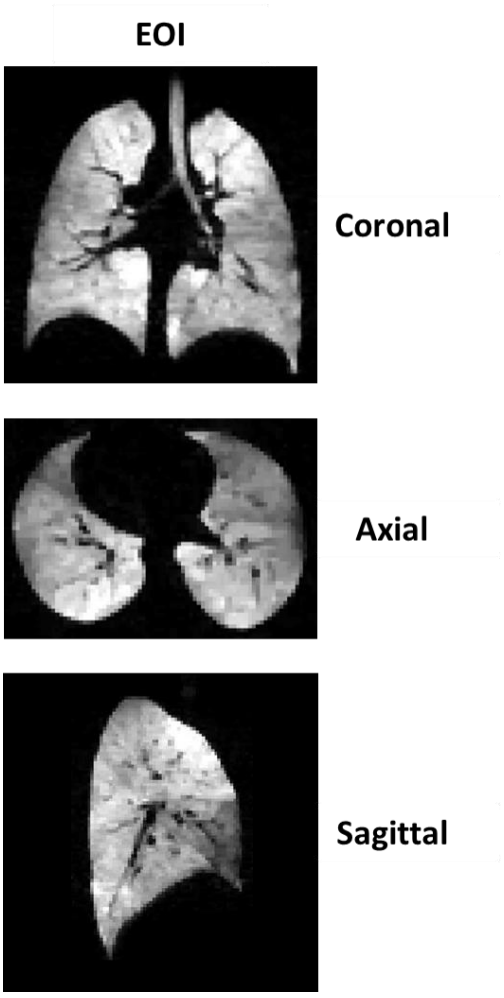

Figure 17: Hyperpolarized Gas Helium-3 Ventilation Magnetic Resonance Images used as reference ventilation images in the evaluation study.Images are acquired at EOI during the hybrid HP gas MR acquisition, ventilation images are shown in all three planes: coronal, axial and sagittal.

5.4.2 DIR-based Ventilation Images

As it was discussed in the beginning of this chapter, this ventilation evaluation study is all MR-based. Therefore, the images that were registered to calculate the ventilation maps were the p-MRI images at EOI and EOE (anatomical lung images). The p-MRIs were deformably registered using the Deformable Multi-Pass algorithm from Velocity AI. As a reminder, Velocity AI is a B-spline deformable image registration algorithm which uses Mutual Information (MI) as its similarity metric. The DIR-based displacement vector field (d-DVF), which mathematically describes the lung tissue deformation between the two respiratory phases on a voxel-by-voxel basis, was extracted for use in the calculation of the regional ventilation surrogate.

Regional lung ventilation was quantified as the regional relative lung volume change between the two respiratory phases (EOE and EOI), and was computed voxel-wise through the Jacobian Determinant of the 3D lung d-DVF which was normalized to the voxel size (4 mm isotropically). The Jacobian method utilized in this study was described in detail in section 3.1.2.1: *Jacobian Determinant*, and enabled us to calculate local volume changes in the lungs from the deformation field. It provides the magnification factor as a result of the transformation of coordinates.

5.4.3 Tagging-based Ventilation Images

For the tagging-based ventilation maps, it is important to emphasize that no DIR was performed. The tagging-based DVF (t-DVF) was measured through the methods

described in section 4.2: *Respiratory Motion* Modeling, by manually tracking the displacement of the center of mass of the evenly distributed ~500 tagged elements in the EOI and EOE tagging MRIs. The sparse DVF measured from the 3D tagged grid pattern in the t-MRIs was interpolated to match the sampling of the v-MRI and p-MRIs and then normalized to voxel size (4 mm) for the ventilation calculation. Finally, the regional ventilation map was quantified as the relative lung volume change between the two respiratory phases (EOI and EOE) and computed voxel-wise through the Jacobian Determinant of the 3D lung t-DVF.

5.4.4 Evaluation

The evaluation consisted on a spatial comparison of all three types of ventilation maps (v-MRI, t-Vent and d-Vent). Given that all images (v-MRI, t-MRI, p-MRI) used to calculate the ventilation maps were acquired in a single breath-hold maneuver with no changes in subject positioning, they were assumed to be spatially co-registered, and thus no additional image registration was necessary for their spatial comparison. For subjects 2, 3 and 4, however, the HP gas ventilation image, v-MRI, and the tagging-based ventilation map, t-Vent, had to be down-sampled from 3.3 x 3.3 x 3.3 mm^3 to 4 x 4 x 4 mm^3 voxel size in order to match the resolution of the DIR-based ventilation map, d-Vent.

All ventilation images were smoothed using a 3 x 3 x 3 voxels Gaussian filter and then normalized to the 90^{th} percentile. Spearman correlation coefficients (r_s) were

computed in a voxel-wise analysis for t-Vent against v-MRI, d-Vent against v-MRI, and d-Vent against t-Vent to measure the monotonic association between them. Spearman coefficients can be between -1 and 1, with 1 being a perfect monotone relationship between the two variables and -1 being a fully opposed correlation

Figure 18 shows the process or workflow used to calculate d-Vent and t-Vent from the proton and tagging images, respectively. This was the process followed to create the ventilation maps for all 4 Subjects in order to then evaluate them with the reference HP gas ventilation images (v-MRI).

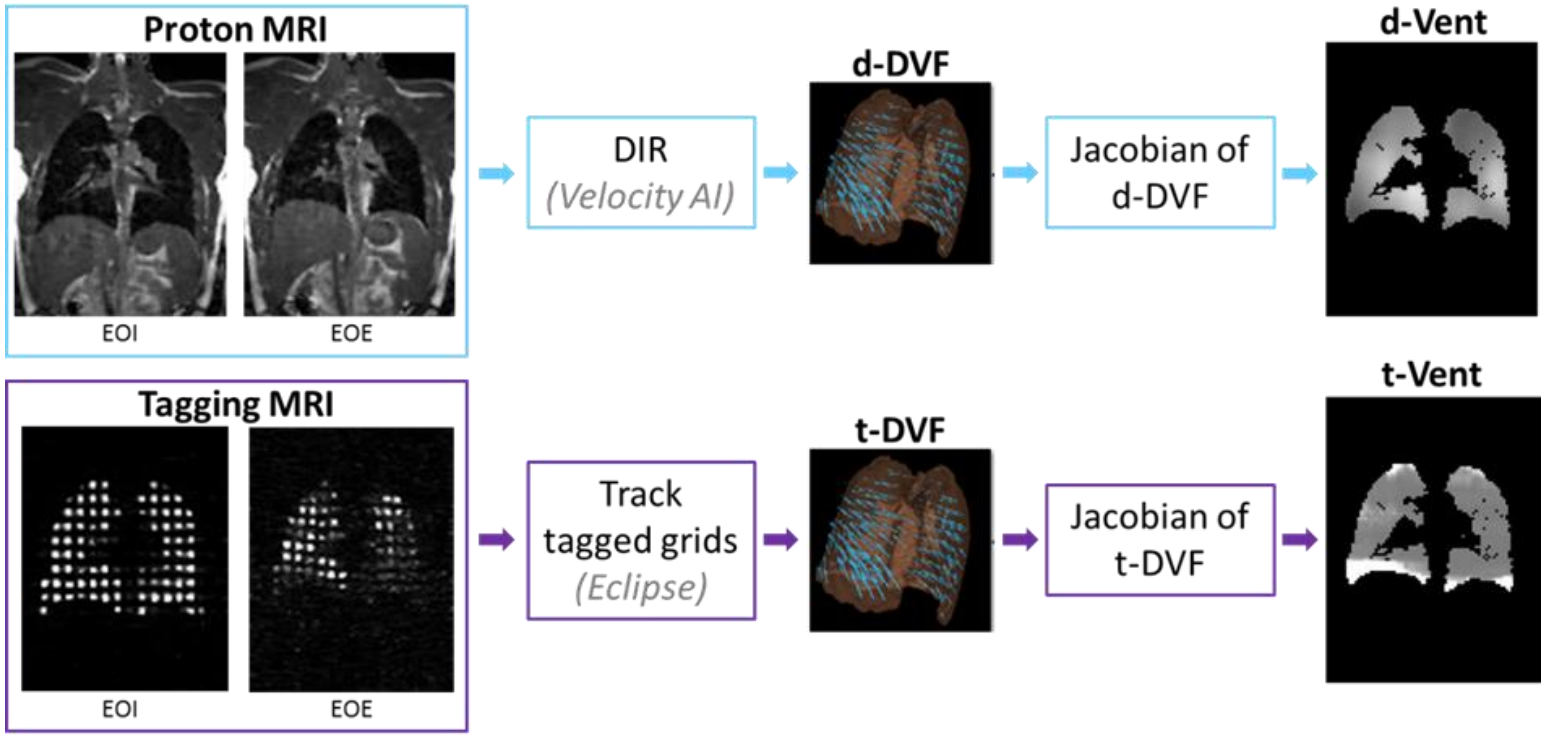

Figure 18: Ventilation evaluation workflow. Proton MR images at EOI and EOE are registered using the Velocity AI DIR algorithm. The d-DVF is then extracted to calculate d-Vent through the Jacobian. For the tagging-based ventilation images, the tagging MR images at EOI and EOE were used to calculate the lung deformation by tracking the displacement of the tagged elements. The displacement vector field t-DVF was utilized to calculate t-Vent through the Jacobian.

5.5 Results

Spearman correlation coefficients for Subject 1 showed the strongest correlation in the three spatial comparisons investigated in this study: t-Vent against v-MRI, d-Vent against v-MRI, and d-Vent against t-Vent with coefficients of $r_s = 0.7$, 0.6 and 0.7, respectively.

Subjects 2 and 3 showed a moderate to strong correlation in all spatial comparisons with coefficients in the range of $r_s = 0.4$ to 0.6 as shown in Table 4. Subject 4 showed moderate correlation for d-Vent against v-MRI with a correlation coefficient of $r_s = 0.5$, but weaker correlation for the spatial comparisons involving the tagging-based ventilation maps, with $r_s = 0.2$ and $r_s = 0.3$ for t-Vent against v-MRI and d-Vent against t-Vent, respectively.

Table 4: Results of the spatial comparison. Table shows the spearman correlation coefficients (r_s) between the Tagging-based Ventilation images and the reference Ventilation MRI (t-Vent vs. v-MRI), the DIR-based Ventilation and the reference Ventilation MRI (d-Vent vs. v-MRI), and between the DIR-based and Tagging-based ventilation images (d-Vent vs. t-Vent).

	Spearman Correlation Coefficients (r_s)		
	t-Vent vs. v-MRI	**d-Vent vs. v-MRI**	**d-Vent vs. t-Vent**
Subject 1	0.71	0.61	0.73
Subject 2	0.50	0.41	0.47
Subject 3	0.57	0.40	0.47
Subject 4	0.20	0.50	0.29

Table 5: Statistical significance of the spatial comparisons. Table shows p-values from the correlation between the Tagging-based Ventilation images and the reference Ventilation MRI (t-Vent vs. v-MRI), the DIR-based Ventilation and the reference Ventilation MRI (d-Vent vs. v-MRI), and between the DIR-based and Tagging-based ventilation images (d-Vent vs. t-Vent) to evaluate statistical significance.

	p-value		
	t-Vent vs. v-MRI	**d-Vent vs. v-MRI**	**d-Vent vs. t-Vent**
Subject 1	0.00	0.00	0.00
Subject 2	0.00	0.00	0.00
Subject 3	0.00	0.00	0.00
Subject 4	0.00	0.00	0.00

The p-values showed statistically significant correlations for all spatial comparisons for all 4 subjects as shown in Table 5. All p-values were essentially zero.

Figure 19 shows the reference HP gas MRI ventilation image and the DIR-based ventilation image (v-MRI and d-Vent) for Subject 1, and Figure 20 shows the regression line plot of correlation for Subject 1 between v-MRI and d-Vent (normalized ventilation maps), which showed strong correlation coefficients.

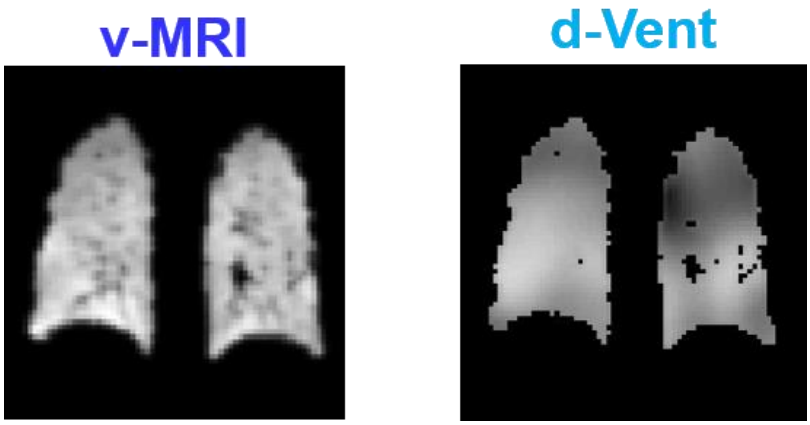

Figure 19: Reference and DIR-based ventilation images for Subject 1: v-MRI and d-Vent.

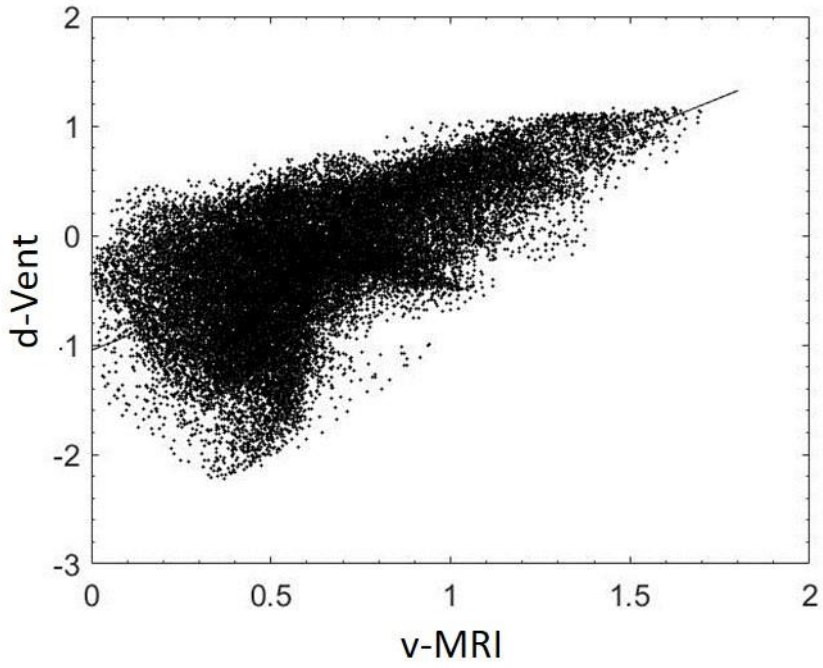

Figure 20: Regression line plot for correlation of v-MRI and d-Vent, Subject 1.

5.6 Discussion

In this study, we developed a technique to spatially compare DIR-based ventilation maps calculated through the Jacobian determinant of the lung d-DVF, Tagging-based ventilation maps calculated through the Jacobian determinant of the lung t-DVF, and reference HP He-3 MRI ventilation images. As mentioned in the Methods and Materials section, all images (p-MRI, t-MRI and v-MRI) were acquired using a novel hybrid MRI technique during a single breath-hold

maneuver and, therefore, all ventilation maps were already spatially co-registered. This is an important aspect and advantage of this investigation since, unlike previous studies, the spatial comparison analysis was not affected by the uncertainties introduced when finding the spatial correspondence between the different ventilation maps, or the variability in patient positioning and respiratory motion reproducibility.

From the spatial comparison analysis, we observed a moderate to strong correlation between all three ventilation maps for 3 out of the 4 subjects investigated, with the fourth subject showing a weak correlation for t-Vent vs. v-MRI and d-Vent vs. t-Vent. Moreover, we observed stronger correlation results from Subject 1 which may be due to the fact that all images for that subject were acquired with the same resolution, and thus no down-sampling was performed which could have affected the correlation results for subjects 2, 3 and 4.

5.7 Conclusion

As more RT clinics incorporate MR imaging for patient simulation, and contouring for treatment planning, this study shows the feasibility of utilizing MR images for DIR-based ventilation calculations. The results of the spatial comparison between the DIR-based and reference ventilation images (d-Vent vs. v-MRI) show moderate to strong spearman correlation coefficients which are higher than many CT

ventilation evaluation studies in the literature.[35,36,50] This may also be due to the fact that the images in this study were acquired during the same breath-hold and therefore inherently co-registered. The tagging-based ventilation maps, t-Vent, which are independent of the accuracy of any DIR algorithms, showed very similar spatial correlations to the reference images, v-MRI, compared to d-Vent. This proves the potential of the Jacobian ventilation calculation method which assumes that local volume changes are an appropriate lung ventilation surrogate.

However, it is essential to consider that these are small human datasets, and therefore it is imperative to extend DIR-validation studies to larger datasets in order to better understand patient or subject variability. Nevertheless, this evaluation study shows promising spatial correlations between transformation-based ventilation methods and a reference ventilation imaging modality.

6. Evaluation of the sensitivity to deformation changes of ventilation and strain as lung functionality metrics

6.1 Purpose

Lung ventilation has been investigated as a metric for functional avoidance treatment planning and treatment response assessment, with several clinical trials[7] being conducted across the country. With the growing interest in incorporating functional information into radiation therapy treatment planning, studies have been exploring a variety of additional functional imaging metrics such as perfusion, gas exchange, elasticity, radiomics feature maps, etc. This study aims to investigate lung strain as an additional metric to assess respiratory mechanics, and compare both (lung ventilation and lung strain) metrics' sensitivity to changes in their deformation fields using Hyperpolarized He-3 Tagging MRI data.

6.2 Methods and Materials

This study utilized physiologically-based respiratory motion models from three subjects to assess the sensitivity of lung strain and lung ventilation by introducing a number of modifications to the DVF, generating new lung function maps, and investigating how much each of these lung function metrics were affected. The DVFs utilized for this study were tagging-based DVFs obtained from the HP gas tagging MRI technique, see Figure 21.

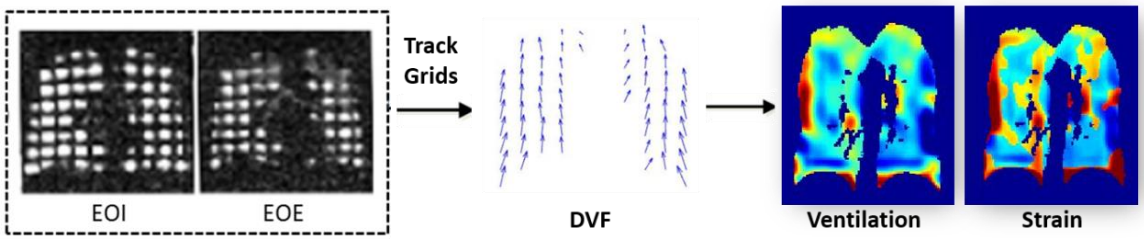

Figure 21: Lung ventilation and lung strain calculation workflow using a tagging-based DVF.

6.2.1 Lung Strain

Deformation-based ventilation studies have not only compared different DIR algorithms, but some research groups have also looked into ventilation surrogates in addition to lung volume changes, such as principal components or lung elasticity metrics.[34,35] This study investigates and assesses the sensitivity to deformation changes of both deformation-based lung ventilation and strain. Strain is defined as the relative deformation of a body due to stress. In one dimension, strain is given by:

$$Strain\ 1D = \frac{\Delta L}{L} \quad (9)$$

where ΔL is the change in length and L is the initial length.

Similar to ventilation, both normal and shear strains can be characterized as relative displacements. The strain-displacement relations in terms of 3 displacement components u, v, w are:

Normal Strains $\epsilon_{xx} = \frac{\partial u}{\partial x}$ $\epsilon_{yy} = \frac{\partial v}{\partial y}$ $\epsilon_{zz} = \frac{\partial w}{\partial z}$ **(10)**

Shear Strains $\gamma_{xy} = \frac{\partial v}{\partial x} + \frac{\partial u}{\partial y}$ $\gamma_{xz} = \frac{\partial w}{\partial x} + \frac{\partial u}{\partial z}$ $\gamma_{yz} = \frac{\partial w}{\partial y} + \frac{\partial v}{\partial z}$ **(11)**

which can be simplified to:

$$Strain = \nabla Displacement \quad \textbf{(12)}$$

Lung strain was computed voxel-wise from the gradient of the tagging-based displacement. Through this algorithm, we obtained a 3x3 tensor that directly measures both the magnitude and direction of the lung deformation and then determines the three principal strains (e1, e2, e3) at each voxel.

Strain Tensor

$$[e] = \begin{bmatrix} e_{11} & e_{12} & e_{13} \\ e_{12} & e_{22} & e_{23} \\ e_{13} & e_{23} & e_{33} \end{bmatrix} = \begin{bmatrix} \varepsilon_x & \frac{1}{2}\gamma_{xy} & \frac{1}{2}\gamma_{xz} \\ \frac{1}{2}\gamma_{xy} & \varepsilon_y & \frac{1}{2}\gamma_{yz} \\ \frac{1}{2}\gamma_{xz} & \frac{1}{2}\gamma_{yz} & \varepsilon_z \end{bmatrix} \quad \textbf{(13)}$$

Figure 22 shows an example of the three principal strain maps for one of the three subjects investigated in this study.

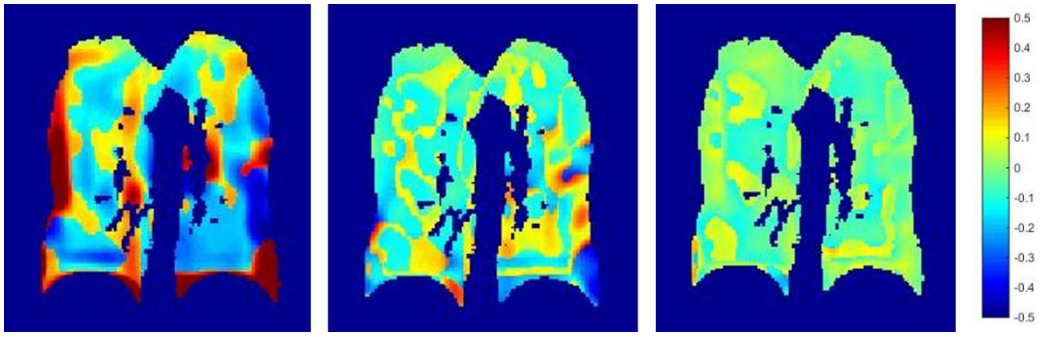

Figure 22: Lung functional strain maps for the three principal strains (e1, e2, and e3, respectively) calculated from the measured t-DVF.

6.2.2 Lung Ventilation

For the lung ventilation calculation, we used the previously described voxel-by-voxel algorithm which was based on computing the Jacobian Determinant of the tagging-based DVF to determine the local volume changes as a ventilation mapping surrogate.

6.2.3 Assessment of sensitivity to deformation changes

Previous studies have investigated the numerical stability of transformation-based ventilation calculations in the past.[51] This study investigates and evaluates the sensitivity of not only ventilation, but also strain maps to deformation changes by manually altering the DVF by a certain percentage (in magnitude or in both magnitude

and direction). Four types of DVF modifications were performed. The mean absolute percent differences of the functional maps generated with the original DVFs versus the maps generated from the modified DVFs were calculated. This workflow is described in Figure 23. The first two types of modifications consisted on uniform changes throughout the entire deformation field. Modifications three and four consisted on implementing random distributions of modifications within a specified interval.

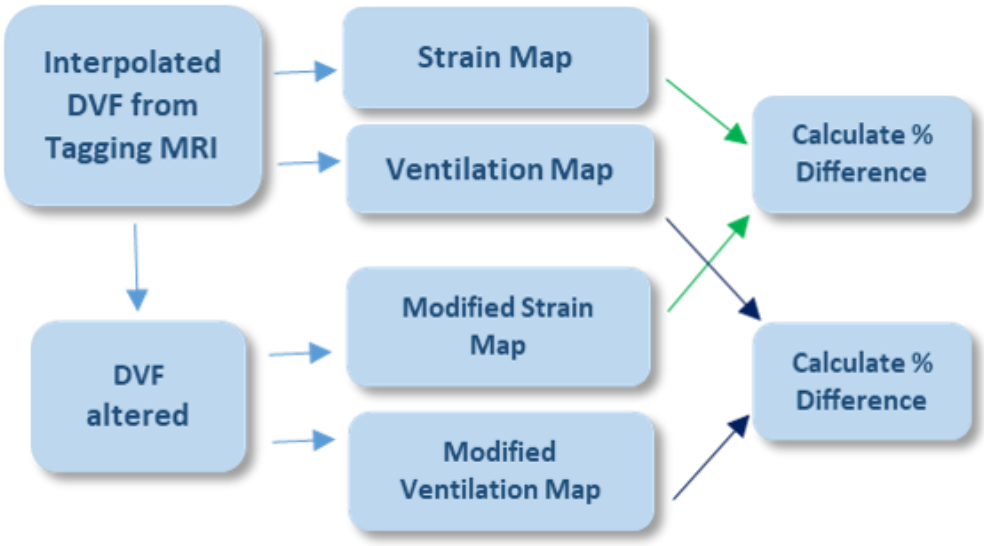

Figure 23: Workflow describing the assessment of sensitivity to deformation changes of ventilation and strain for lung functional mapping using HP gas tagging MRI data.

6.3 Results

The first type of modification consisted of a uniform magnitude change in all 3 DVF directions or vector components (Dx, Dy, Dz). The DVF's vector component magnitudes were changed by a certain percentage: 25, 50, 75, and 100%. Table 6 shows the mean of the absolute percent differences within the lungs between original strain and ventilation maps compared to the altered maps where changes in DVF magnitude by 25, 50, 75 and 100% were performed for each of the three subjects. The graph in Figure 24 shows the average values among all three subjects for easier visualization.

Uniform DVF Modifications performed:

- Dx, Dy, Dz: 25%
- Dx, Dy, Dz: 50%
- Dx, Dy, Dz: 75%
- Dx, Dy, Dz: 100%

The second type of modification consisted of not only introducing a change in DVF magnitude, but also a directional change in the DVF by changing the vector component magnitudes by different percentages. Table 7 shows the mean of the absolute percent differences within the lungs between original strain and ventilation maps compared to the altered maps where changes in DVF magnitude and direction were performed for each of the three subjects. The graph in Figure 25 shows the average values among all three subjects for easier visualization.

Uniform DVF Modifications with directional change:

- Dx: 25%, Dy: 50%, Dz: 75%
- Dx: 50%, Dy: 75%, Dz: 25%
- Dx: 75%, Dy: 25%, Dz: 50%

The third and fourth types of DVF modifications consisted of introducing a random distribution of changes throughout the DVF within a given interval (0-25%, 0-50%, 0-75%, 0-100%). This was achieved using a random number generator within the set interval.

Random DVF Modifications within given interval:

- Dx, Dy, Dz: 0-25%
- Dx, Dy, Dz: 0-50%
- Dx, Dy, Dz: 0-75%
- Dx, Dy, Dz: 0-100%

Random DVF Modifications with directional change within given interval:

- Dx: 0-25%, Dy: 0-50%, Dz: 0-75%
- Dx: 0-50%, Dy: 0-75%, Dz: 0-25%
- Dx: 0-75%, Dy: 0-25%, Dz: 0-50%

Table 8 shows the mean of the absolute percent differences within the lungs between original strain and ventilation maps compared to the altered maps where randomly distributed changes in DVF were performed by a percentage within the

intervals: 0-25%, 0-50%, 0-75%, 0-100% for each of the three subjects. The graph in Figure 26 shows the average values among all three subjects for easier visualization.

Table 9 shows the mean of the absolute percent differences within the lungs between original strain and ventilation maps compared to the altered maps where random changes in DVF magnitude and direction were performed by a percentage within the intervals: 0-25%, 0-50%, 0-75%, 0-100% for each of the three subjects. The graph in Figure 27 shows the average values among all three subjects for easier visualization.

These results show much larger mean absolute percent differences between original and modified ventilation maps compared to the principal strain maps for all tests performed in this study; ranging from an average of 49.5 to 2743.7% for ventilation and 30.6 to 650.0% for strain among the 3 subjects. The principal strain maps showed much smaller average standard deviations between subjects.

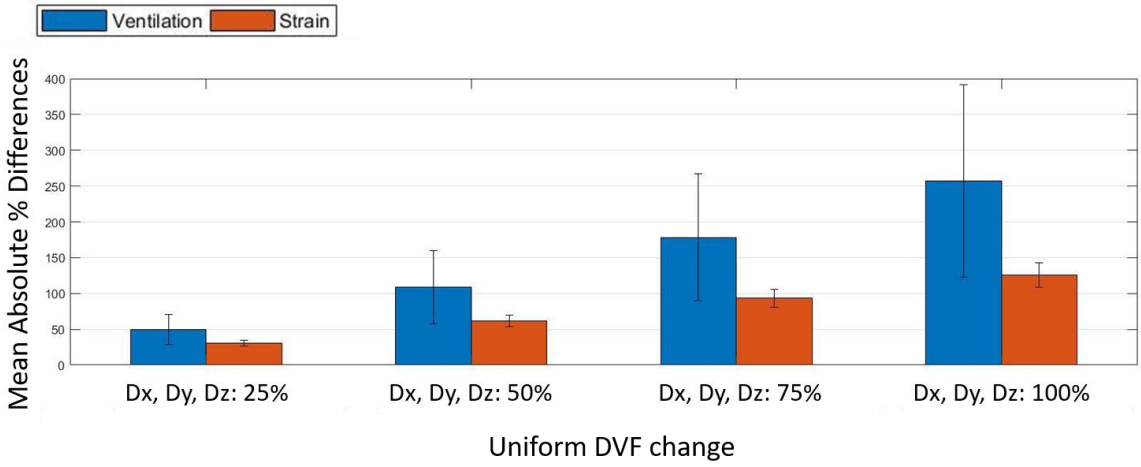

Figure 24: Mean absolute percent differences between original and modified ventilation and strain maps. Modified maps had a <u>uniform</u> DVF magnitude modification in the Dx, Dy, and Dz components indicated by the percentages in the x-axis. These are average differences for all 3 subjects.

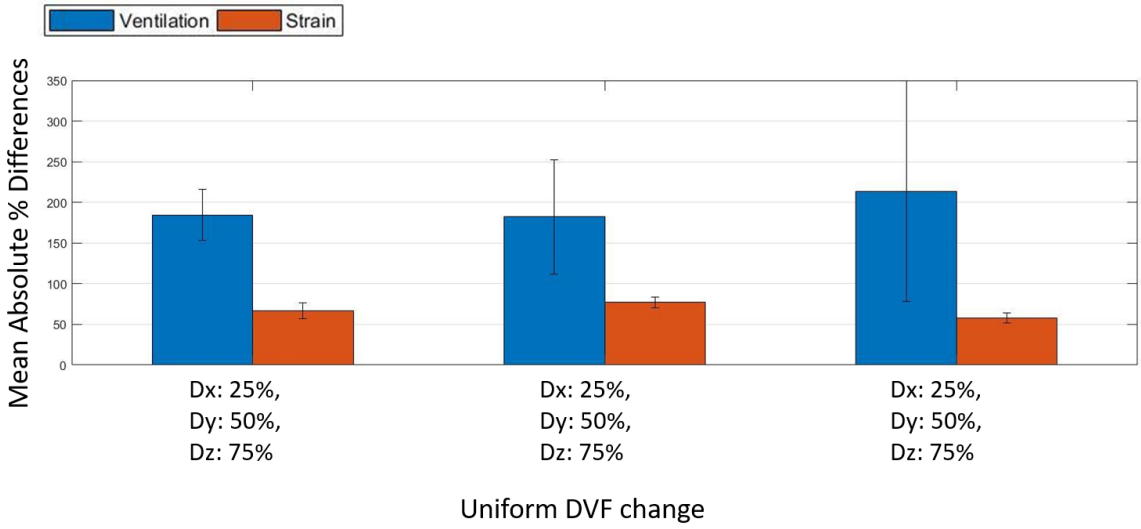

Figure 25: Mean absolute percent differences between original and modified ventilation and strain maps. Modified maps had a <u>uniform</u> DVF magnitude <u>and direction</u> modification in the Dx, Dy, and Dz components indicated by the percentages in the x-axis. These are average differences for all 3 subjects.

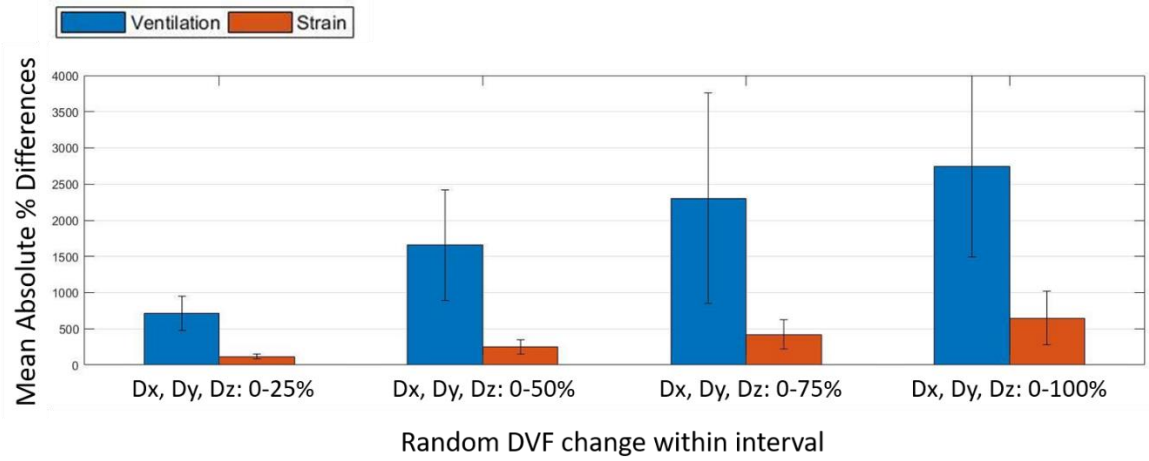

Figure 26: Mean absolute percent differences between original and modified ventilation and strain maps. Modified maps had a random distribution of DVF magnitude modifications in the Dx, Dy, and Dz components within intervals indicated by the percentages in the x-axis.

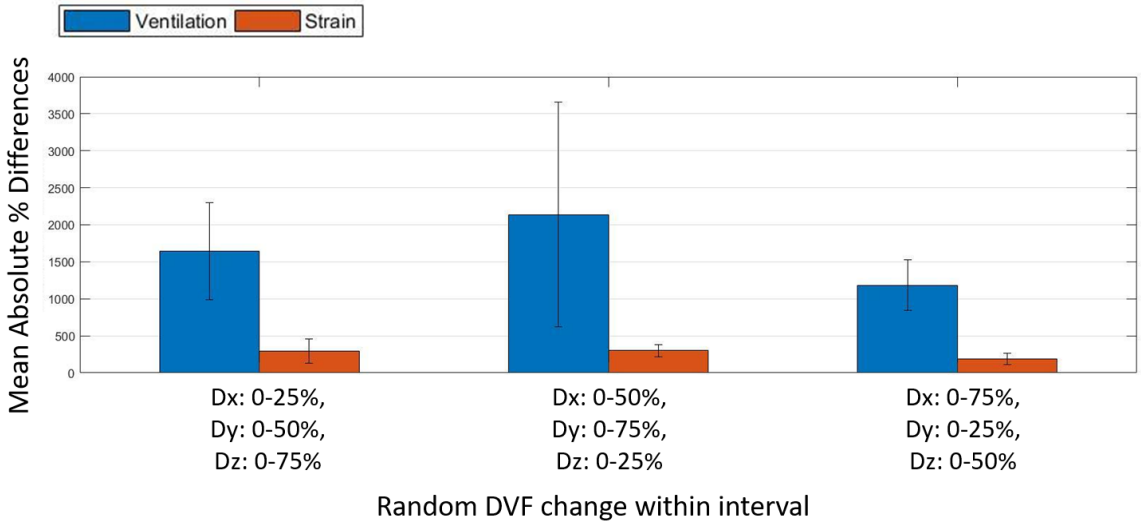

Figure 27: Mean absolute percent differences between original and modified ventilation and strain maps. Modified maps had a random distribution of DVF magnitude and directional modifications in the Dx, Dy, and Dz components within the intervals indicated by the percentages in the x-axis.

Table 6: Results from uniform changes in DVF magnitude. Table shows the mean absolute percent differences between original strain and ventilation maps compared to altered maps; changes in DVF magnitude by 25, 50, 75 and 100% were performed.

	DVF Uniform Magnitude Change	Dx, Dy, Dz: 25%	Dx, Dy, Dz: 50%	Dx, Dy, Dz: 75%	Dx, Dy, Dz: 100%
		Mean of the Absolute Percent Differences (%)			
Subject 1	Ventilation	44.1	95.9	155.2	222.0
	Strain	34.3	69.6	105.9	143.5
Subject 2	Ventilation	73.0	165.2	276.2	405.7
	Strain	30.4	61.1	92.5	125.0
Subject 3	Ventilation	31.4	65.8	103.2	143.7
	Strain	27.1	54.4	81.6	108.9
Average	**Ventilation**	**49.5**	**109.0**	**178.2**	**257.1**
	Strain	**30.6**	**61.7**	**93.3**	**125.8**
Std. Deviation	**Ventilation**	**21.3**	**51.0**	**88.8**	**134.5**
	Strain	**3.6**	**7.6**	**12.2**	**17.3**

Table 7: Results from uniform changes in DVF magnitude and direction. Table shows mean absolute percent differences between original strain and ventilation maps compared to altered maps; changes in DVF magnitude and direction by 25, 50, 75 and 100% were performed.

	DVF Uniform Magnitude and Directional Change	Dx: 25%, Dy: 50%, Dz: 75%	Dx: 50%, Dy: 75%, Dz: 25%	Dx: 75%, Dy: 25%, Dz: 50%
		Mean of the Absolute Percent Differences (%)		
Subject 1	Ventilation	205.8	145.7	147.3
	Strain	77.2	83.3	64.3
Subject 2	Ventilation	198.8	262.9	369.1
	Strain	63.8	77.4	57.1
Subject 3	Ventilation	148.5	138.1	125.0
	Strain	58.4	70.2	52.4
Average	**Ventilation**	**184.4**	**182.2**	**213.8**
	Strain	**66.5**	**77.0**	**58.0**
Std. Deviation	**Ventilation**	**31.3**	**70.0**	**135.0**
	Strain	**9.7**	**6.6**	**6.0**

Table 8: Results from random changes in DVF magnitude. Table shows the mean absolute percent differences between original strain & ventilation maps compared to the altered maps where random changes in DVF magnitude were performed within the intervals: 0-25%, 0-50%, 0-75%, 0-100%.

	DVF Random Magnitude Change Within Interval	Dx, Dy, Dz: 0-25%	Dx, Dy, Dz: 0-50%	Dx, Dy, Dz: 0-75%	Dx, Dy, Dz: 0-100%
		Mean of the Absolute Percent Differences (%)			
	Ventilation	595.9	1592.3	1557.5	2075.9
Subject 1	Strain	155.3	359.3	655.6	1066.9
	Ventilation	983.5	2453.1	3976.8	4185.1
Subject 2	Strain	103.1	214.1	348.9	515.7
	Ventilation	556.7	932.0	1381.8	1970.1
Subject 3	Strain	87.2	172.9	265.1	367.4
	Ventilation	**712.0**	**1659.1**	**2305.4**	**2743.7**
Average	**Strain**	**115.2**	**248.8**	**423.2**	**650.0**
	Ventilation	**235.9**	**762.7**	**1450.2**	**1249.4**
Std. Deviation	**Strain**	**35.6**	**97.9**	**205.6**	**368.6**

Table 9: Results from random changes in DVF magnitude & direction. Table shows the mean absolute percent differences between original strain & ventilation maps compared to the altered maps where random changes in DVF magnitude and direction were performed within the intervals: 0-25%, 0-50%, 0-75%, 0-100%.

	DVF Random Magnitude and Directional Change within interval	Dx: 0-25%, Dy: 0-50%, Dz: 0-75%	Dx: 0-50%, Dy: 0-75%, Dz: 0-25%	Dx: 0-75%, Dy: 0-25%, Dz: 0-50%
		Mean of the Absolute Percent Differences (%)		
Subject 1	Ventilation	1661.0	1311.4	1410.3
	Strain	480.08	385.2	273.1
Subject 2	Ventilation	2291.3	3888.5	1348.8
	Strain	223.26	290.8	147.7
Subject 3	Ventilation	979.1	1210.7	796.0
	Strain	177.1	221.0	132.4
Average	**Ventilation**	**1643.8**	**2136.9**	**1185.0**
	Strain	**293.5**	**299.0**	**184.4**
Std. Deviation	**Ventilation**	**656.3**	**1517.8**	**338.3**
	Strain	**163.2**	**82.4**	**77.2**

6.4 Conclusion

From the results shown in Figures 24-27 and Tables 6-9, we can see that the Tagging-based ventilation maps calculated through the Jacobian of the DVF might be more sensitive to deformation changes compared to the lung strain maps, showing much larger mean absolute percent differences between the original and modified maps. This could indicate two things, while ventilation might be more sensitive to smaller deformation changes which could be an advantage, this could also indicate that it is more sensitive to small errors or uncertainties in the DVF which could make the calculation more numerically unstable compared to strain. Studies have investigated the numerical stability of the Jacobian ventilation calculation using CT images,[51] and therefore, these results provide us with an insight on how these two metrics compare to each other in an MR-based study.

For future studies, it would be interesting to spatially compare the reference HP gas ventilation images to strain maps calculated through the workflows established in this dissertation to investigate how well these two metrics correlate with each other.

7. Conclusion

7.1 Dissertation Conclusions

This study is the first, to our knowledge, to evaluate deformation-based ventilation methods using an all MR based dataset, and to incorporate a novel tagging-based ventilation mapping method into the evaluation. As MRI becomes a more popular imaging modality in the field of radiation therapy with more centers acquiring MR-LINACs and MR simulators, through the completion of these aims, we have proved the feasibility of using proton MR images for transformation-based ventilation calculations. Previous studies have found poorer correlation coefficients when comparing CT-based ventilation methods to hyperpolarized gas MR imaging techniques.[36] In this dissertation, we have established a workflow to create lung respiratory motion models through a novel HP tagging MRI. It was found that there can be significant differences in the deformation fields when comparing these models to DIR-based DVFs. Therefore, the inclusion of biomechanical information based on the extraction of landmarks, tissue characteristics, or other physiological information could potentially be incorporated into DIR algorithms to yield improved results. Furthermore, this dissertation established the workflow to calculate Jacobian-based ventilation maps from both proton and tagging MRIs, and to evaluate them against a reference modality – HP gas ventilation MR. These aims were achieved using a very unique dataset from a novel hybrid MR image acquisition technique which yielded promising results with improved correlations.

7.2 Future Efforts

Future efforts include extending these studies to a larger dataset. Additionally, expanding this workflow to test the reproducibility of these ventilation calculations using images acquired from the same subject, from different respiratory cycles, would give us an important insight on the effect that respiratory motion reproducibility can have on these calculations.[52]

Moreover, it would be interesting to investigate the spatial correlation between the reference HP Gas Ventilation MR images and lung strain maps to see how lung strain maps compare to the DIR-based and tagging-based ventilation results.

Furthermore, an important limitation to recognize about these studies is that these image sets are acquired from healthy volunteers, so it would be key to test the feasibility of these methods on radiation oncology patients, to see if the workflow for the spatial comparisons established in this dissertation would yield similar results.

References

1. Siegel RL, Miller KD, Jemal A. Cancer statistics, 2020. *CA Cancer J Clin*. 2020;70(1):7-30. doi:10.3322/caac.21590

2. Marks LB, Bentzen SM, Deasy JO, et al. Radiation Dose-Volume Effects in the Lung. *Int J Radiat Oncol Biol Phys*. 2010;76(3 SUPPL.):S70. doi:10.1016/j.ijrobp.2009.06.091

3. Vinogradskiy Y, Castillo R, Castillo E, Chandler A, Martel M, Guerrero T. TU-A-BRC-11: Use of Weekly 4DCT-Based Ventilation Maps to Quantify Changes in Lung Function for Patients Undergoing Radiation Therapy. *Med Phys*. 2011;38(6):3744. doi:10.1118/1.3613087

4. Yamamoto T, Kabus S, Von Berg J, Lorenz C, Keall PJ. Impact of four-dimensional computed tomography pulmonary ventilation imaging-based functional avoidance for lung cancer radiotherapy. *Int J Radiat Oncol Biol Phys*. 2011;79(1):279-288. doi:10.1016/j.ijrobp.2010.02.008

5. Yaremko BP, Guerrero TM, Noyola-Martinez J, et al. Reduction of Normal Lung Irradiation in Locally Advanced Non-Small-Cell Lung Cancer Patients, Using Ventilation Images for Functional Avoidance. *Int J Radiat Oncol Biol Phys*. 2007;68(2):562-571. doi:10.1016/j.ijrobp.2007.01.044

6. Cai J, McLawhorn R, Altes TA, et al. Helical tomotherapy planning for lung cancer based on ventilation magnetic resonance imaging. *Med Dosim*. 2011;36(4):389-396. doi:10.1016/j.meddos.2010.09.008

7. Vinogradskiy Y, Rusthoven CG, Schubert L, et al. Interim Analysis of a Two-Institution, Prospective Clinical Trial of 4DCT-Ventilation-based Functional Avoidance Radiation Therapy. *Int J Radiat Oncol Biol Phys*. 2018;102(4):1357-1365. doi:10.1016/j.ijrobp.2018.07.186

8. Roos JE, Mcadams HP, Kaushik SS, Driehuys B, Justus : Hyperpolarized Gas MRI: Technique and Applications HHS Public Access. *Magn Reson Imaging Clin N Am*. 2015;23(2):217-229. doi:10.1016/j.mric.2015.01.003

9. Madani I, De Ruyck K, Goeminne H, De Neve W, Thierens H, Van Meerbeeck J. Predicting risk of radiation-induced lung injury. *J Thorac Oncol*. 2007;2(9):864-874. doi:10.1097/JTO.0b013e318145b2c6

10. Faught AM, Miyasaka Y, Kadoya N, et al. Evaluating the Toxicity Reduction With Computed Tomographic Ventilation Functional Avoidance Radiation Therapy. *Int J Radiat Oncol Biol Phys*. 2017;99(2):325-333. doi:10.1016/j.ijrobp.2017.04.024

11. Faught AM, Yamamoto T, Castillo R, et al. Evaluating Which Dose-Function Metrics Are Most Critical for Functional-Guided Radiation Therapy. *Int J Radiat Oncol Biol Phys*. 2017;99(1):202-209. doi:10.1016/j.ijrobp.2017.03.051

12. Hoover DA, Capaldi DP, Sheikh K, et al. *Functional Lung Avoidance for Individualized Radiotherapy (FLAIR): Study Protocol for a Randomized, Double-Blind Clinical Trial*.; 2014. doi:10.1186/1471-2407-14-934

13. Exchanging Oxygen and Carbon Dioxide - Lung and Airway Disorders - Merck Manuals Consumer Version. https://www.merckmanuals.com/home/lung-and-airway-disorders/biology-of-the-lungs-and-airways/exchanging-oxygen-and-carbon-dioxide. Accessed March 15, 2020.

14. Dancer R, Thickett D. Pulmonary function tests. *Medicine (Baltimore)*. 2012;40(4):186-189. doi:10.1016/j.mpmed.2012.01.009

15. Office-Based Spirometry: Key to Diagnosing Rural COPD Patients - The Rural Monitor. https://www.ruralhealthinfo.org/rural-monitor/office-based-spirometry/. Accessed March 13, 2020.

16. Restrictive lung disease - wikidoc. https://www.wikidoc.org/index.php/Restrictive_lung_disease. Accessed April 13, 2020.

17. Jögi J, Jonson B, Ekberg M, Bajc M. Ventilation-perfusion SPECT with 99mTc-DTPA versus Technegas: a head-to-head study in obstructive and nonobstructive disease. *J Nucl Med*. 2010;51(5):735-741. doi:10.2967/jnumed.109.073957

18. Roach PJ, Schembri GP, Bailey DL. V/Q scanning using SPECT and SPECT/CT. *J Nucl Med*. 2013;54(9):1588-1596. doi:10.2967/jnumed.113.124602

19. Bajc M, Neilly B, Miniati M, Mortensen J, Jonson B. Methodology for ventilation/perfusion SPECT. *Semin Nucl Med*. 2010;40(6):415-425. doi:10.1053/j.semnuclmed.2010.07.002

20. Bajc M, Jonson B. Ventilation/perfusion SPECT - An essential but underrated method for diagnosis of pulmonary embolism and other diseases. *Eur J Nucl Med*

Mol Imaging. 2009;36(5):875-878. doi:10.1007/s00259-009-1125-x

21. Kent M, Wisner E, Johnson L, Stern J. Combined assessment of pulmonary ventilation and perfusion with single-energy computed tomography and image processing. :1-32.

22. Galbán CJ, Han MK, Boes JL, et al. Computed tomography-based biomarker provides unique signature for diagnosis of COPD phenotypes and disease progression. *Nat Med*. 2012;18(11):1711-1715. doi:10.1038/nm.2971

23. Galban C, Boes J, Hoff B, et al. Evaluation of parametric response mapping for monitoring COPD subtypes. *Eur Respir J*. 2014;44(Suppl 58).

24. Labaki WW, Gu T, Murray S, et al. Voxel-Wise Longitudinal Parametric Response Mapping Analysis of Chest Computed Tomography in Smokers. *Acad Radiol*. 2019;26(2):217-223. doi:10.1016/j.acra.2018.05.024

25. Capaldi DPI, Zha N, Guo F, et al. Pulmonary Imaging Biomarkers of Gas Trapping and Emphysema in COPD: ^{3} He MR Imaging and CT Parametric Response Maps. *Radiology*. 2016;279(2):597-608. doi:10.1148/radiol.2015151484

26. Pompe E, Van Rikxoort EM, Schmidt M, et al. Parametric response mapping adds value to current computed tomography biomarkers in diagnosing chronic obstructive pulmonary disease. *Am J Respir Crit Care Med*. 2015;191(9):1084-1086. doi:10.1164/rccm.201411-2105LE

27. Altes TA, Mata J, De Lange EE, Brookeman JR, Mugler JP. Assessment of lung development using hyperpolarized helium-3 diffusion MR imaging. *J Magn Reson Imaging*. 2006;24(6):1277-1283. doi:10.1002/jmri.20723

28. Mugler JP, Altes TA. Hyperpolarized 129Xe MRI of the human lung. *J Magn Reson Imaging*. 2013;37(2):313-331. doi:10.1002/jmri.23844

29. Oh S, Kim S. Deformable image registration in radiation therapy. *Radiat Oncol J*. 2017;35(2):101-111. doi:10.3857/roj.2017.00325

30. Castillo R, Castillo E, Martinez J, Guerrero T. Ventilation from four-dimensional computed tomography: Density versus Jacobian methods. *Phys Med Biol*. 2010;55(16):4661-4685. doi:10.1088/0031-9155/55/16/004

31. Ding K, Cao K, Fuld MK, et al. Comparison of image registration based measures

of regional lung ventilation from dynamic spiral CT with Xe-CT. *Med Phys*. 2012;39(8):5084-5098. doi:10.1118/1.4736808

32. Du K, Bayouth JE, Ding K, Christensen GE, Cao K, Reinhardt JM. Reproducibility of intensity-based estimates of lung ventilation. *Med Phys*. 2013;40(6):063504. doi:10.1118/1.4805106

33. Vinogradskiy Y, Castillo R, Castillo E, et al. Use of 4-Dimensional Computed Tomography-Based Ventilation Imaging to Correlate Lung Dose and Function With Clinical Outcomes. *Int J Radiat Oncol Biol Phys*. 2013;86(2). doi:10.1016/j.ijrobp.2013.01.004

34. Cui T, Huang Q, Miller WG, Zhong X, Yin F, Cai J. Evaluation of Lung Ventilation and Strain From Direct Measurements of Lung Deformation During Breathing Using Hyperpolarized Helium-3 Tagging MRI. *Int J Radiat Oncol*. 2014;90(1):S143-S144. doi:10.1016/j.ijrobp.2014.05.610

35. Kipritidis J, Tahir BA, Cazoulat G, et al. The VAMPIRE challenge: A multi-institutional validation study of CT ventilation imaging. *Med Phys*. 2019;46(3):1198-1217. doi:10.1002/mp.13346

36. Tahir BA, Hughes PJC, Robinson SD, et al. Spatial Comparison of CT-Based Surrogates of Lung Ventilation With Hyperpolarized Helium-3 and Xenon-129 Gas MRI in Patients Undergoing Radiation Therapy. *Int J Radiat Oncol Biol Phys*. 2018;102(4):1276-1286. doi:10.1016/j.ijrobp.2018.04.077

37. Reinhardt JM, Ding K, Cao K, Christensen GE, Hoffman EA, Bodas S V. Registration-based estimates of local lung tissue expansion compared to xenon CT measures of specific ventilation. *Med Image Anal*. 2008;12(6):752-763. doi:10.1016/j.media.2008.03.007

38. Guerrero T, Sanders K, Noyola-Martinez J, et al. Quantification of regional ventilation from treatment planning CT. *Int J Radiat Oncol Biol Phys*. 2005;62(3):630-634. doi:10.1016/j.ijrobp.2005.03.023

39. Guerrero T, Sanders K, Castillo E, et al. Dynamic ventilation imaging from four-dimensional computed tomography. *Phys Med Biol*. 2006;51(4):777-791. doi:10.1088/0031-9155/51/4/002

40. Zhang GG, Latifi K, Du K, et al. Evaluation of the ΔV 4D CT ventilation calculation method using in vivo xenon CT ventilation data and comparison to

other methods. *J Appl Clin Med Phys*. 2016. doi:10.1120/jacmp.v17i2.5985

41. Hegi-Johnson F, Keall P, Barber J, Bui C, Kipritidis J. Evaluating the accuracy of 4D-CT ventilation imaging: First comparison with Technegas SPECT ventilation. *Med Phys*. 2017. doi:10.1002/mp.12317

42. Simon BA. *NON-INVASIVE IMAGING OF REGIONAL LUNG FUNCTION USING X-RAY COMPUTED TOMOGRAPHY*. Vol 16.; 2000.

43. Cai J, Altes TA, Miller GW, et al. MR grid-tagging using hyperpolarized helium-3 for regional quantitative assessment of pulmonary biomechanics and ventilation. *Magn Reson Med*. 2007;58(2):373-380. doi:10.1002/mrm.21288

44. Hu L, Huang Q, Cui T, et al. A hybrid proton and hyperpolarized gas tagging MRI technique for lung respiratory motion imaging: A feasibility study. *Phys Med Biol*. 2019;64(10). doi:10.1088/1361-6560/ab160c

45. Qing K, Altes TA, Tustison NJ, et al. Rapid acquisition of helium-3 and proton three-dimensional image sets of the human lung in a single breath-hold using compressed sensing. *Magn Reson Med*. 2015;74(4):1110-1115. doi:10.1002/mrm.25499

46. Garrison W, Qing K, Tafti S, et al. Highly Accelerated Dynamic Acquisition of 3D Grid-Tagged He-3 Lung Images Using Compressed Sensing. *ISMRM 2018, Proc*. 2018. http://archive.ismrm.org/2018/4462.html. Accessed March 15, 2020.

47. Mooney KE, Miller GW, Dolph PA, et al. *A 3-Liter Capacity, Hybrid Spin-Exchange 3 He Polarizer for Medical Imaging*.

48. Brock KK. Results of a Multi-Institution Deformable Registration Accuracy Study (MIDRAS). *Int J Radiat Oncol Biol Phys*. 2010;76(2):583-596. doi:10.1016/j.ijrobp.2009.06.031

49. Yushkevich PA, Piven J, Hazlett HC, et al. User-guided 3D active contour segmentation of anatomical structures: Significantly improved efficiency and reliability. *Neuroimage*. 2006;31(3):1116-1128. doi:10.1016/j.neuroimage.2006.01.015

50. Yamamoto T, Kabus S, Lorenz C, et al. WE-C-WAB-04: Comparison of 4D-CT Ventilation Imaging with SPECT Ventilation Imaging for Thoracic Cancer Patients. In: *Medical Physics*. ; 2013. doi:10.1118/1.4815540

51. Castillo E, Castillo R, Vinogradskiy Y, Guerrero T. The numerical stability of transformation-based CT ventilation. *Int J Comput Assist Radiol Surg*. 2017;12(4):569-580. doi:10.1007/s11548-016-1509-x

52. Woodruff HC, Shieh CC, Hegi-Johnson F, Keall PJ, Kipritidis J. Quantifying the reproducibility of lung ventilation images between 4-Dimensional Cone Beam CT and 4-Dimensional CT. *Med Phys*. 2017. doi:10.1002/mp.12199

Biography

Isabella Duarte was born in Mexico and moved to the United States to begin her undergraduate education at Seton Hall University in Spring 2012. She graduated from Seton Hall University as Valedictorian of the Class of 2015, with a Bachelor of Science in Physics and a Minor in Applied Scientific Mathematics. In August 2015, Isabella entered the Duke University Medical Physics Graduate Program as a Ph.D. student working under the advisement of Dr. Jing Cai and Dr. Fang-Fang Yin in the Radiation Therapy track. She completed her Ph.D. degree in Medical Physics in May 2020. Isabella has presented her research at the American Association of Physicists in Medicine (AAPM) Annual Meetings, and several research symposiums. In Fall 2018, she studied abroad at the Hong Kong Polytechnic University participating in a Research Attachment Programme. During her graduate studies at Duke, Isabella has also received multiple honors, scholarships and awards including the Chancellor's Scholarship and the Dean's Graduate Fellowship from Duke University, as well as the James T. Dobbins III Leadership Award and the Excellence in Teaching Assistantship Award from the Duke University Medical Physics Graduate Program. She has also received fellowships from the National Institute of Health (NIH) including the prestigious F31 Diversity Kirschstein NRSA Fellowship and a Research Supplement to Promote Diversity in Health-Related Research.